Title
Nano- and Micro- Technology Approaches to Enhance Drug Delivery

Author
Levy, Elizabeth

Publication Date
2019

Peer reviewed|Thesis/dissertation

Nano- and Micro- Technology Approaches to Enhance Drug Delivery

by
Elizabeth Levy

DISSERTATION
Submitted in partial satisfaction of the requirements for degree of
DOCTOR OF PHILOSOPHY

in

Pharmaceutical Sciences and Pharmacogenomics

in the

GRADUATE DIVISION
of the
UNIVERSITY OF CALIFORNIA, SAN FRANCISCO

Approved:

DocuSigned by:
Tejal Desai
5D917BC35F4B4A0...

Tejal Desai

Chair

DocuSigned by:
Deanna Kroetz

Deanna Kroetz

DocuSigned by:
Shuvo Roy
C1B7512AE288433...

Shuvo Roy

Committee Members

ACKNOWLEDGMENTS

Thank you to my friends and family for their support during my PhD. I would like to thank my advisors, Tejal Desai and Deanna Kroetz, for their constant support throughout my PhD journey along with fostering a collaborative and productive lab environment. I am grateful for Tejal's and Deanna's encouragement to attend conferences and to spend a summer interning in an industry environment to allow me to figure out my future career path. Tejal has been a great mentor, always giving me freedom to pursue my interests. Deanna has also been a great mentor and very supportive working through *in vivo* problems and planning experiments for hours at a time.

I am thankful to the Desai lab members who have always been supportive and who I have truly made lasting relationships with, Priya Mohindra, Gauree Chendke, William Lykins, Yiqi Cao, Joel Finbloom, Ryan Chang, and Xiao Huang. I have thoroughly enjoyed going to lab everyday to work alongside my colleagues and friends in a fun and productive environment. Priya has been a great friend always willing to lend a hand and lead lab bonding activities. Gauree as my fellow gaucho; I have enjoyed all of our great conversation in lab. As we joined the lab the same year, I am grateful for the support of Will and Yiqi and all of our "3rd" year meetings. Ryan has been a great mentor, very supportive and caring about the research and my personal growth. I am thankful to have the pleasure to sit next to Joel in lab. I have enjoyed all our random conversation from dog videos to scientific discussion, it has been a great balance with work and fun. Thank you, Xiao, for all the scientific conversations.

I would like to especially thank Karen Samy. Karen has been one of my closest friends in lab. Karen and I worked together on 2 projects, and I have had a great time working and collaborating with someone who is very knowledgeable and naturally inquisitive. From our

coffee breaks in “our area” to working in cell culture together, Karen has strongly influenced my PhD and I am grateful to have the opportunity to know her.

I would also like to thank Colin Zamecnik, my graduate student mentor when I rotated in Desai lab. Colin has been very influential in my growth and success in my graduate studies. From rock climbing to long days doing animal work, Colin has always been extremely supportive and a great friend. Colin has been a great mentor, always willing to spend time helping me and other lab members.

Everyone in my program, PSPG, has been great and supportive. I would especially like to thank Emmalyn and Majorie for being great study friends our first year in the program together. I am grateful I was able to interact and become friends with such fun, great, and smart people during my PhD. With our dinner and lunch sessions to get advice on situations and vent about any issues we were having, I am grateful for the time we have spent over the last 5 years.

I want to thank my fiancé William Fox and our dog Leia. William has been an incredible support system and has been great about emphasizing a good work life balance. Weekends hiking or climbing have been a great break from thinking about work. Leia has been the best dog always eager and happy to spend time hanging out with me during my long nights writing. No matter how disappointing the day was, coming home to a happy dog makes everything significantly better.

My parents and family have been extremely supportive during my PhD. My parents have helped me and supported my decision to enter science against all of their business backgrounds. My grandma has been a great support to make sure I am always happy with what I am doing.

CONTRIBUTIONS

Chapter 1 was modified from "Reversible Inhibition of Efflux Transporters by Hydrogel Microdevices" as it was published in the *European Journal of Pharmaceutics and Biopharmaceutics* in 2019. Elizabeth Levy and Karen Samy contributed to study design. Execution and analyses were carried out by Elizabeth Levy, Karen Samy, and Nicholas Lamson. Elizabeth Levy wrote the manuscript with contributions from Deanna Kroetz and Tejal Desai.

Chapter 2 was modified from a manuscript in preparation "Innate Activating Nanoparticles Lead to Activation of Antigen Presenting Cells to Reduce Tumor Burden". Elizabeth Levy, Ryan Chang, and Colin Zamecnik contributed to study design. Execution and analyses were carried out by Elizabeth Levy, Ryan Chang, and Colin Zamecnik. Elizabeth Levy wrote the manuscript with contributions from Ryan Chang.

Chapter 3 was modified from a manuscript in preparation "Tissue-Factor Targeted Benzo-Resolvin and Resolvin D1 Loaded Nanoparticles to Locally Deliver Anti-Inflammatory Compounds Following Vascular Intervention". Elizabeth Levy and Evan Werlin contributed to study design. Execution and analyses were carried out by Elizabeth Levy and Evan Werlin. Elizabeth Levy wrote the manuscript.

Nano- and Micro- Technology Approaches to Enhance Drug Delivery

Elizabeth Levy

ABSTRACT

Small molecules and protein therapeutics are constantly being developed due to their high potency and biological function, but there are many barriers that reduce the therapeutic efficacy of these compounds such as a short half-life leading to high clearance, and biological degradation. As a result, to overcome these challenges higher doses have to be administered with increased frequency to reach a therapeutically relevant concentration. To address these issues nano- and micro- technology has been utilized to increase drug absorption. This dissertation presents various approaches to drug delivery based on the disease target, application, and therapeutic compound. We showed that hydrogel microdevices reversibly inhibit intestinal efflux transporters P-glycoprotein and Breast Cancer Resistance Protein, resulting in an increase in drug absorption. We demonstrated in a Caco-2 model that this decrease in efflux transporter function was due to a decreased amount of transporter present on the cell surface in the presence of microdevices. Also, presented are two polymer nanoparticle-based systems designed for different disease targets. First, for cancer immunotherapy we designed a nanoparticle loaded with an adjuvant cocktail with a tumor specific peptide to promote antigen presenting cell activation and downstream tumor specific T cell activation. Therapeutically, these drug-loaded nanoparticles were able to decrease tumor volume in a subcutaneous melanoma model and melanoma foci in a metastasis model. Second, in atherosclerosis where arteries were damaged, we showed that tissue factor peptide targeted nanoparticles loaded with an anti-inflammatory agent were able to target desired damaged arteries where tissue factor is typically exposed. The

strategies presented here expand the application of nano- and micro- technology for design and implementation in a variety of different diseases and targets. We have shown increased drug absorption and efficacy not only by increased drug half-life but by targeted therapeutics to desired regions resulting in increased local concentrations.

TABLE OF CONTENTS

LIST OF FIGURES

LIST OF TABLES

CHAPTER 1: Reversible Inhibition of efflux transporters by hydrogel microdevices[*]

Abstract

Oral drug delivery is a preferred administration route due to its low cost, high patient compliance and fewer adverse events compared to intravenous administration. However, many pharmaceuticals suffer from poor solubility and low oral bioavailability. One major factor that contributes to low bioavailability are efflux transporters which prevent drug absorption through intestinal epithelial cells. P-glycoprotein (P-gp) and Breast Cancer Resistance Protein (BCRP) are two important efflux transporters in the intestine functioning to prevent toxic materials from entering systemic circulation. However, due to its broad substrate specificity, P-gp limits the absorption of many therapeutics, including chemotherapeutics and antibacterial agents. Methods to inhibit P-gp with competitive inhibitors have not been clinically successful. Here, we show that micron scale devices (microdevices) made from a commonly used biomaterial, polyethylene glycol (PEG), inhibit P-gp through a biosimilar mucus in Caco-2 cells and that transporter function is restored when the microdevices are removed. Microdevices were shown to inhibit P-gp mediated transport of calcein AM, doxorubicin, and rhodamine 123 (R123) and BCRP mediated transport of BODIPY-FL-prazosin. When in contact with Caco-2 cells, microdevices decrease the cell surface amount of P-gp without affecting the passive transport. Moreover, there was an increase in mucosal to serosal transport of R123 with microdevices in an *ex-vivo* mouse model and increased absorption *in vivo*. This biomaterial-based approach to inhibit efflux transporters can be applied to a range of drug delivery systems and allows for a nonpharmacologic method to increase intestinal drug absorption while limiting toxic effects.

[*] Modified from the publication: Levy, E. et.al (2018) Reversible Inhibition of efflux transporters by hydrogel microdevices. *Eur J Pharm and Biopharm* **123:**502-514.

Introduction

Oral drug dosing is the preferred route of delivery due to its convenience, safety, and low cost.[1–4] However, many drugs suffer from poor solubility and low oral bioavailability which can limit their therapeutic effectiveness. Factors that contribute to low bioavailability are the low pH of the stomach, intestinal metabolizing enzymes leading to drug degradation, and the hydrophobic mucosal layer and efflux transporters preventing intestinal drug absorption. [1,5] Efflux transporters of the multigene ATP binding cassette (ABC) transporter family such as P-glycoprotein (P-gp), breast cancer resistance protein (BCRP), and multidrug resistance-associated protein 2 (MRP2) are expressed on the apical membrane of intestinal epithelial cells.[6] These transporters efflux absorbed compounds from the intestinal cells back into the gastrointestinal (GI) lumen, thus preventing them from reaching the systemic circulation.[6] Efflux transporters function to protect the small intestine from harmful toxins and xenobiotics by limiting their absorption.[7,8] However, most efflux transporters have broad substrate specificity which translates into poor oral bioavailability for a significant number of therapeutics.[6,8–10]

Many strategies have been employed to inhibit the function of efflux transporters to increase drug absorption.[7,11,12] P-gp is the most widely studied efflux transporter since it limits the bioavailability of numerous substrates, including chemotherapeutics, immunosuppressants and antimicrobial agents.[7] The main approaches studied for P-gp inhibition include competitive inhibitors that directly block the site of drug binding and noncompetitive inhibitors that either block the hydrolysis of adenosine triphosphate (ATP) necessary for P-gp function or allosterically interact to reduce P-gp activity.[7,13–15] However, decades of research aimed at targeting P-gp through the use of chemical inhibitors provide limited evidence for clinical applicability.[16,17] The lack of success using P-gp inhibitors to improve bioavailability underlies

the ongoing search for safer and more effective methods to address this critical limitation in oral absorption.[15]

Micro- and nanotechnology-based drug delivery systems have been used as effective tools to increase drug absorption and enhance bioavailability.[4,18] Previously, we have shown that nanostructured thin films increase drug permeation through the intestinal epithelium.[19] We have also shown that microdevices increase residence time in the intestine and increase permeation, thus increasing drug bioavailability.[20] Additionally, hydrogels are widely used in drug delivery because of their biocompatibility, ease of tunability, and their ability to increase bioavailability, thus allowing for improved absorption in target regions.[21–25] In particular, PEG hydrogels are commonly used for oral drug delivery as PEG is non-immunogenic and biocompatible.[26–28] PEG based nanoparticles have been investigated for their ability to modulate permeability *in vitro*. [23] Additionally, PEG in a non-crosslinked form was shown to limit P-gp activity with evidence indicating the changes are due to alterations in the microenvironment of P-gp.[29] Altering the molecular weight of the non-crosslinked PEG has been shown to alter the degree of P-gp inhibition; however, there is not a clear correlation between PEG molecular weight and P-gp inhibition.[30,31] Hydrogel and polymer based microparticles, however, have a decreased residence time in the intestine which is limited by peristaltic flow that dislodges the hydrogel material.[32]

The overall goal of this study is to investigate the effects of hydrogel microdevices to improve drug absorption through gastrointestinal epithelial cells. Since PEG-based hydrogels are commonly used in various controlled release systems, gaining a basic understanding of their effects on efflux transporters is essential for the development of improved oral delivery systems. Biocompatible PEG-based drug delivery microdevices were developed and optimized for adherence to the intestinal epithelial wall and reversible inhibition of efflux transport. The data

presented below supports this approach for maximizing drug absorption, increasing oral bioavailability, and limiting toxicity of orally administered substrates of P-gp and BCRP.

Materials & Methods

Fabrication of microdevices

Microdevices with a diameter of 200 μm and a thickness of 20 μm were fabricated as previously described.[33] Briefly, a solution consisting of 80% w/v 750 number average molecular weight (Mn) polyethylene glycol dimethacrylate (PEGDMA) (Sigma-Aldrich), 10% w/v IRCAGURE (2-Hydroxy-4′-(2-hydroxyethoxy)-2-methylpropiophenone) (Sigma-Aldrich) in dimethyl sulfoxide (DMSO), and 10% w/v deionized water was added to the surface of a piranha cleaned 3" silicon wafer (Addison Engineering Inc) at a thickness of 20 μm. The wafer is brought into contact with a photomask with 200 μm exposed features and irradiated with a 365 nm UV light source using a Karl Suss Mask Aligner for 1 minute to crosslink the PEGDMA. The solution viscosity is important for appropriate spreading on the wafer. The wafer is then removed and the polymer that is not crosslinked is washed away in water. The microdevices are then removed from the wafer into ethanol. Prior to studies, microdevices are washed with sterile 2% Bovine Serum Albumin (BSA) solution (Sigma-Aldrich).

Cell culture

Human colon adenocarcinoma cell line (Caco-2) purchased from ATCC was maintained in 2D cell culture as previously described.[19] Caco-2 cells between passage 5 and 13 were used for all experiments. Mycoplasma test was performed on the cell line and found to be negative. Cell culture experiments are performed in two formats, on transwells and 96 well plates. Cells are seeded at $75*10^3$ cells/cm^2 and cultured for 21 days for transwell experiments. For

experiments performed in a 96 well plate, cells are seeded at $27*10^3$ cells/cm^2 and cultured for 14 days. Cell growth conditions were optimized so that P-gp expression levels between the transwells and 96 well plates were similar.

Immunohistochemistry

Caco-2 cells cultured on transwells for 21 days were fixed as described previously.[19] DAPI (1:500) and Alexa 488 Phalloidin (1:200) (Life Technologies 1726566) were used to stain the cells. After staining, transwells were cut out and mounted on a slide with slowfade gold antifade reagent with DAPI (Invitrogen). Cells were imaged with a Tokagawa CSU22 spinning disk confocal microscope.

Transwell culture

Caco-2 cells were seeded at $75*10^3$ cells/cm^2 on high density polycarbonate Transwell inserts (24-well, 0.4 uM pore size) (Corning) as described previously.[19] Cells were cultured for 21 days before use in experiments.

Viability studies

Caco-2 cells were seeded at a density of $27*10^3$ cells/cm^2 on a 96 well plate. After 14 days of culture the cells were washed, and a PrestoBlue assay was performed. Briefly, microdevices were added to the wells and incubated for 3 hours. The microdevices were removed and PrestoBlue cell viability Reagent (Invitrogen) added to the wells. After a 10-minute incubation at 37°C the absorbance was read at 570 nm. Wells without microdevices were used as controls.

Dead cells were measured by propidium iodine (PI) staining. Cells were grown in a transwell for 21 days, after which microdevices were added for 3 hours. The cells were lifted by

cell dissociation buffer and stained with 2 mg/mL PI for 5 minutes. The cells were washed 3X and placed in 2% BSA solution to run on flow cytometry (BD FACS Calibur).

An ATP assay kit (Abcam) was used to determine total levels of cellular ATP in Caco-2 cells grown on a transwell model for 21 days. Cells were treated in the absence or presence of microdevices for 3 hours. After 3 hours, phenol red free Minimum Essential Medium (MEM) (Gibco) is removed and detergent is added to lyse cells and stabilize ATP. Substrate solution provided by the kit is added and luminescence is measured after 15 minutes.

Transport studies

The calcein AM assay was performed in a 96 well plate. Caco-2 cells were grown on 96 well plates for 2 weeks. After the cells were washed with phenol red free MEM, 3 μM calcein AM in the presence and absence of microdevices or CSA, positive control inhibitor of P-gp, was added to the wells and incubated at 37°C. After 1 or 3 hours the cells were lysed to determine the intracellular calcein concentration. Cellular levels of calcein were normalized to protein determined by a micro bicinchoninic acid (BCA) protein assay kit (ThermoFisher). To test active vs passive transport, the calcein AM assay was run at 4°C.

Prior to transport experiments, cells were washed with phenol red free MEM. The following substrates were added to the basolateral chamber to measure P-gp or BCRP transport: 5 μM rhodamine 123 (R123) (Invitrogen), 10 μg/mL doxorubicin (LC Laboratories) or 5 μM BODIPY-FL-prazosin (Invitrogen). The microdevices, 15 μM CSA (Sigma-Aldrich), or 50 μM Ko143 (Sigma-Aldrich) were added to the apical chamber and incubated at 37°C. CSA and Ko 143 are small molecule positive control inhibitors for P-gp and BCRP, respectively. The apical chamber was sampled over time and the fluorescence was measured using excitation (nm)/emission (nm) 495/560 (R123), 490/590 (doxorubicin), or 485/530 (prazosin). To account

for passively absorbed drug in the microdevices, the microdevices were removed after the experiment and placed in an eppendorf tube. The microdevices are centrifuged at 500 g for 4 minutes and the supernatant is removed, sampled, and the fluorescence is measured. Fresh buffer is added to wash the microdevices. This process is repeated until there is no detectable fluorescence in the supernatant. The amount of drug absorbed into the microdevices was accounted for in calculating the amount of drug transported. Transport function recovery was studied after microdevice removal. The control, positive control, and microdevice wells were washed and phenol red free MEM was added to the apical chamber. The fluorescence in the apical chamber was sampled and measured over time. The apparent permeability coefficient was calculated according to the equation:

$$P_{app} = \left(\frac{dQ}{dt}\right) * \left(\frac{1}{AC_o}\right)$$

where P_{app} is the apparent permeability (cm/s), dQ/dt (μg/s) is rate of drug transport, A is surface area of the transwell, and C_0 (μg/mL) is the initial drug concentration. Transwells without microdevices were used as controls. Transepithelial electrical resistance (TEER) is measured at each time point. Apical to basal transport is studied by adding the drug substrate at the concentrations indicated above to the apical chamber with the microdevices or positive control inhibitors. The basal chamber is then sampled and analyzed.

Biosimilar mucus transport study

Biosimilar mucus consisting of 5% (w/v) mucin, 0.11% (w/v) linoleic acid, 0.36% (w/v) cholesterol, 0.18% (w/v) phosphatidylcholine, 0.163% (w/v) polysorbate 80, and 3.1% (w/v) BSA was prepared based on previously described methods.[34] Biosimilar mucus at 250 μL/cm^2, which is approximately 2 mm in thickness, was placed on the cultured Caco-2 cells in transwells. The mucus was incubated for 1 hour prior to the addition of microdevices, phenol red free MEM

(control), or CSA in the apical chamber and 5 μM R123 in the basolateral chamber. Transport assays were performed as described above. After the experiment was complete, the mucus layer was removed and the microdevices were visualized on the Caco-2 cells by microscopy.

Passive permeability

The passive transport of 4kDa FITC Dextran (Sigma-Aldrich) across the Caco-2 cell monolayer was performed as previously shown.[35] Briefly, Caco-2 cells well grown on transwells for 21 days. FITC Dextran (2 mM, 4kDa) was added to the apical chamber with and without microdevices. The basal chamber was sampled, and the fluorescence was measured over time (Ex 485 nm/Em 530 nm). All experiments were done in triplicate at 37°C.

Flow cytometry of cell surface P-gp

The cell surface P-gp was labeled with fluorescent anti-P-gp monoclonal antibody (BD, Clone 17F9) and analyzed by flow cytometry. Briefly, Caco-2 cells grown on transwells for 21 days were washed with phenol red free MEM. Microdevices were added to the apical chamber for 3 hours at 37°C. After 3 hours, the cells were removed from the transwell membrane with cell dissociation buffer. The cells were washed 3X and then incubated with Alexa Fluor 488-conjugated mouse anti-P-gp monoclonal antibody at 4°C for 30 min. The cells were then washed 3X with 2% BSA and analyzed by flow cytometry. Two transwells were combined for each sample to increase the cell number for flow cytometry. Transwells without microdevices were used as controls.

mRNA expression of efflux transporters

Microdevices were added to transwells cultured with Caco-2 cells for 21 days. After 3 hours, RNA was collected from the transwell using RNeasy Mini kit (Qiagen). cDNA was generated from RNA with iScript cDNA Synthesis Kit (Bio-Rad). qPCR reactions were

performed with SYBR Green PCR Master Mix (Applied Biosystems). L19 is used as a reference control. Samples are compared to transwells without microdevices as a treatment control.

Table 1.1: Gene and Primer Sequence for qPCR

Gene	**Primer Sequence**
MDR1	F 5'-GCC AAA GCC AAA ATA TCA GC 3' R 5'-TTC CAA TGT GTT CGG CAT 3'
ABCG2	F 5'-TGC AAC ATG TAC TGG CGA AGA 3' R 5'-TCT TCC ACA AGC CCC AGG 3'
L19	F 5'-TCGCCTCTAGTGTCCTCCG 3' R 5'- GCGGGCCAAGGTGTTTTTC 3'

***Ex-vivo* mouse model**

Three BALB/c mice were sacrificed at 18-20 weeks of age. Jejenum of the intestine was isolated and solid waste was removed. The jejenum was sectioned into 4 cm long pieces. One end of the intestine was closed with a suture and 5 μM R123 was pipetted into the intestine section containing microdevices, CSA, or a control without treatment on the mucosal side. The other end of the intestine was tied off before the start of the experiment. The intestinal sacs were incubated in a 24 well plate in media at 37°C. The solution on the serosal side was removed, replaced with fresh media, and the fluorescence was measured at excitation 495 nm /emission 560 nm over time. After the final sample was taken, the intestine was removed and measured to determine the surface area.

Mouse studies

All mouse experiments were approved by the institutional animal care and use committee (IACUC) at Carnegie Mellon University (Pittsburgh, PA, USA) under protocol number PROTO201600017, and were performed in accordance with all institutional, local, and federal regulations. C57BL/6 mice were either purchased from Charles River Laboratories (Wilmington, MA, USA) or obtained from an institutionally managed breeding colony. Prior to experiments, mice were housed in cages of no more than five animals, with controlled temperature (25°C), 12

hour light-dark cycles, and free access to food and water. Mice utilized in this study were male and 8 – 16 weeks old (16 – 26 grams). The free-to-use PS power calculator (Vanderbilt) was used to determine the minimal sample size for which statistical power was greater than or equal to 0.8. (n = 5 – 7). Mice were fasted for 12 hours the night before an experiment to limit the variability caused by food matter and feces in the GI tract. Oral gavages and phosphate buffered saline (PBS) rehydration were administered at a volume of 10 ml solution per kg of mouse body weight (10 μL/g).

Oral delivery of rhodamine 123

Fasted mice were orally gavaged with one of three treatment solutions: 40,000 microdevices/mL solution (400,000 microdevices/kg total dose), 0.5 mg/mL (5 mg/kg) cyclosporine A (CSA) as a positive control, or phosphate buffer saline (PBS) as a negative control. Every treatment also contained 9.6 mg/mL (96 mg/kg) BSA to stabilize the solution. Thirty minutes (controls) or two hours (microdevices) later, submandibular blood was collected from each mouse to provide baseline fluorescent values, and each mouse received a gavage of 0.4 mg/mL (4 mg/kg) R123. Submandibular blood was collected at 10, 20, 30, and 60 minutes following the R123 gavage, and mice received subcutaneous PBS rehydration after the 30 and 60 minute blood draws. At 240 minutes, the mice were euthanized and final blood collected via cardiac puncture.

All samples were centrifuged to isolate the serum, which was removed and examined for R123 concentration by reading for fluorescence on a Tecan Spark® automated plate reader (495/560 nm). Application of a R123 calibration curve, in the presence of mouse serum, yielded the reported concentrations of the model drug in each sample.

Statistics

Statistical analysis was performed by a two-way ANOVA with a Tukey's multiple comparison correction to determine significance between groups. Analysis between two groups was performed by a two-tailed t-test. Plots show mean ± standard deviation (SD) where * represents $p<0.05$, ** represents $p<0.01$, and *** represents $p<0.001$.

Results and Discussion

Microdevice characterization

Uniform 200 μm biocompatible PEG microdevices were fabricated by photolithography. Briefly, PEGDMA, deionized water, and initiator (IRGACURE) were mixed and a thin layer was added to a silicon wafer. The mixture was irradiated through a 200 μm mask to form crosslinked microdevices (Figure 1.1A). Microdevices were visualized with bright field microscopy (20 μm x 200 μm) (Figure 1.1B). Microdevices did not alter cell viability or metabolic activity as indicated by staining of dead cells with propidium iodide (PI) and with a Presto Blue assay which measured the reducing power of living cells (Figure 1.2A). The microdevices also did not affect ATP amounts, indicating viable cells (Figure 1.2A).

In Figure 1.2B, microdevices were visualized on top of cells with confocal microscopy. Microdevices were added for 3 hours on a Caco-2 monolayer grown on transwells for 21 days. Immunostaining shows an intact confluent monolayer of Caco-2 cells expressing actin underneath the devices (Figure 1.2B).

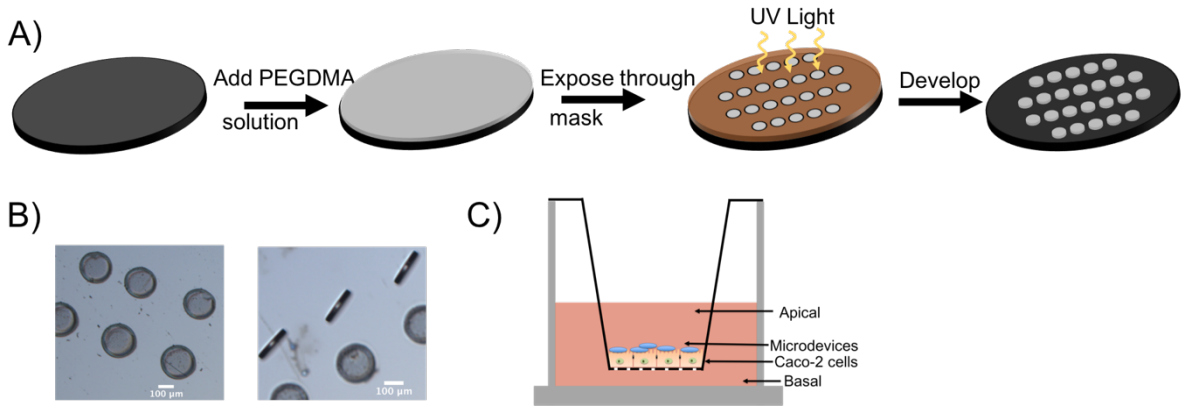

Figure 1.1: Fabrication of PEGDMA microdevices using photolithography. A) Schematic representation of the microdevice formation using ultraviolet (UV) light irradiation. B) Brightfield (5X) image of microdevices. Scale bar 100 µm. C) Transwell model system with Caco-2 cells grown on transwell insert membrane for 21 days and microdevices added to the apical surface of the intestinal monolayer.

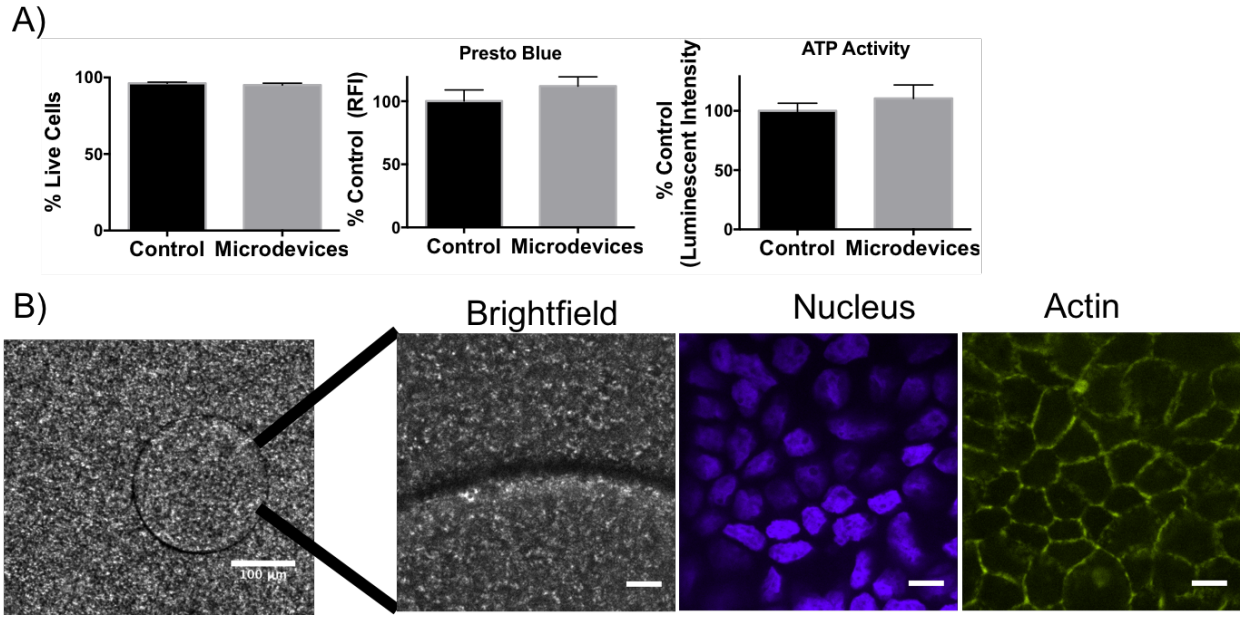

Figure 1.2: Characterization of microdevices in Caco-2 cells. A) Biocompatibility studies of the microdevices on Caco-2 cells with a propidium iodide (dead) stain, PrestoBlue assay, and ATP assay (two-tailed t-test, Mean ± SD; n=3). B) Fluorescence confocal images (10X) of microdevice (Scale Bar =100 µm) and of microdevices incubated for 3 hours on Caco-2 cells grown on transwells for 3 weeks (60X) showing the microdevices in brightfield (BF), DAPI nucleus (blue) stain, and phalloidin actin (green) (representative image of n=3 wells). Scale Bar =10 µm.

Microdevice inhibition of efflux transporters

Efflux transporters decrease oral bioavailability by pumping drugs that get absorbed into the intestinal cells back out into the GI lumen, preventing drugs from entering the systemic circulation.[6] First, the effects of the microdevices on P-gp function were tested. P-gp is a critical efflux transporter in the intestine with a broad substrate specificity and a determinant of oral bioavailability of many drug substrates from chemotherapeutics to immunosuppressants.[7] Microdevices were shown to inhibit the transport of multiple model P-gp substrates, including calcein AM, doxorubicin, and R123. Calcein AM, a non-fluorescent P-gp substrate that freely diffuses into the cell is rapidly cleaved intracellularly by esterases to form fluorescent calcein, which is not a P-gp substrate. Inhibition of P-gp results in an accumulation of calcein AM inside the cell and a corresponding increase in hydrolysis to calcein and higher fluorescence. Microdevices (3000 microdevices/cm^2) increased the intracellular concentration of calcein to a similar degree as a positive control small molecule inhibitor, CSA, indicating P-gp inhibition (Figure 1.3A). P-gp inhibition by microdevices was also studied in a transwell system where the Caco-2 cells were cultured on transwell membrane inserts for 21 days (Figure 1.1C). The TEER at the time of study was greater than 350 $\Omega \bullet cm^2$, indicating tight epithelial junctions. Doxorubicin is a chemotherapeutic which freely diffuses into the cell when added to the basal chamber and then gets transported by P-gp into the apical chamber. Microdevices at 3000 microdevices/cm^2 were placed on the Caco-2 cells in a transwell decreased efflux of doxorubicin into the apical chamber, consistent with P-gp inhibition (Figure 1.3B). The apparent permeability (P_{app}) is defined by the drug transport rate, initial drug concentration, and the surface area of the transwell insert. P_{app} decreased in Caco-2 cells with the microdevices or when treated with CSA (Table 1.2). The P-gp substrate R123 was also tested in Caco-2 transwells. R123 was added to

the basolateral chamber and transported into the cell where it is subsequently effluxed into the apical chamber by P-gp. We tested whether the level of inhibition was dependent on the dose of microdevices with the addition of 3000 microdevices/cm^2 or 900 microdevices/cm^2 to the apical chamber. While we have seen significant decrease of R123 with both doses compared to control, the 3000 microdevices/cm^2 showed a higher degree of inhibition more similar to CSA (Figure 1.3C). The P_{app} decreased with the microdevices and CSA (Table 1.2). To test whether the microdevices permanently alter transporter function, we performed a transporter recovery assay. R123 transport by P-gp recovered following removal of the microdevices to levels comparable to cells without microdevices, indicating reversible inhibition of P-gp (Figure 1.3D). Reversibility of transporter function is important as these efflux transporters function to prevent toxic material from entering systemic circulation. Therefore, permanently decreasing transporter function could result in toxic adverse effects.[7,8]

Since there is significant overlap between P-gp and BCRP substrates, the effects of the microdevices on BCRP function were also tested using the BCRP substrate BODIPY-FL-prazosin (prazosin). Prazosin freely diffuses into the cell and is effluxed out on the apical membrane by BCRP. As a positive control we used a potent BCRP specific inhibitor, Ko143. Microdevices (3000 microdevices/cm^2) decreased basal to apical transport (Figure 1.4) and decreased the prazosin P_{app} to a similar degree as Ko143 (Table 1.2). As shown previously, efflux transporters often work in concert with each other, with one efflux transporter increasing function in response to loss of function of another efflux transporter, thus limiting drug absorption.[36] Inhibition of both P-gp and BCRP by the hydrogel microdevices is predicted to enhance the increase in intestinal absorption.

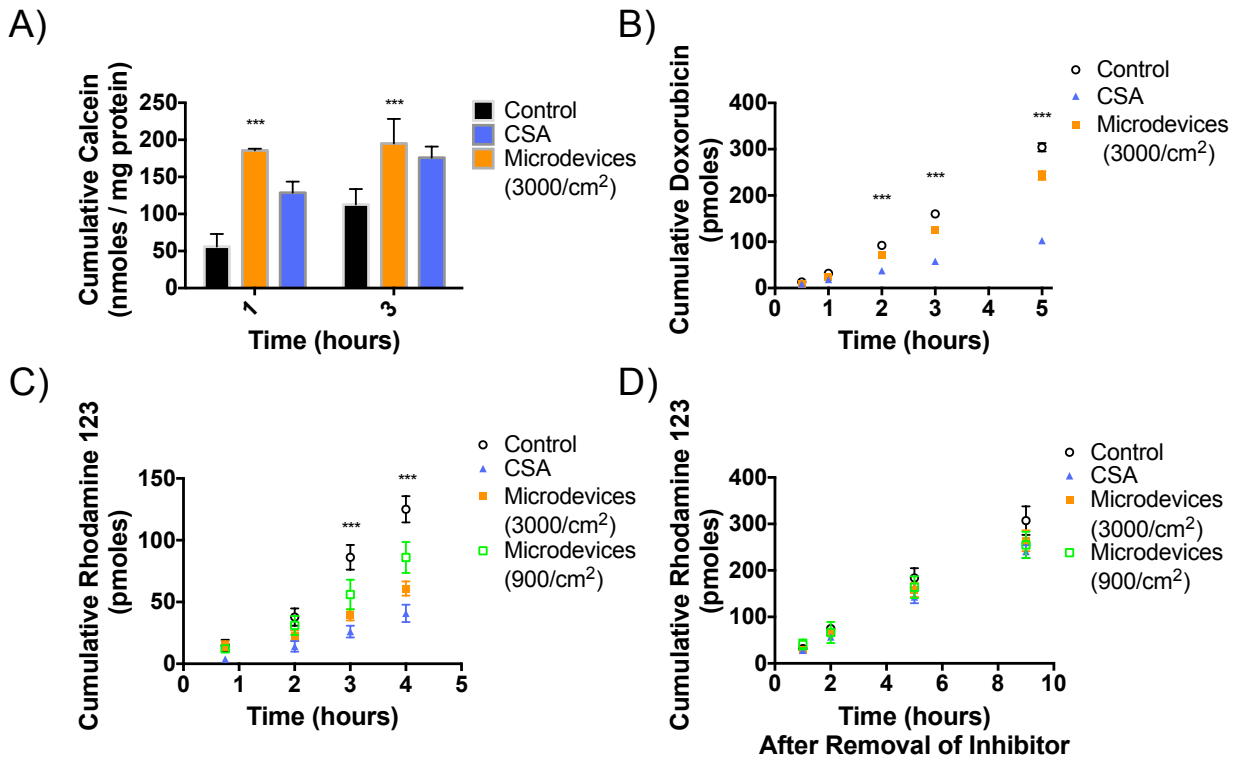

Figure 1.3: Inhibition of P-gp transport by microdevices in Caco-2 cells. A) Caco-2 cells were grown on 96 well plates for 14 days before measurement of intracellular calcein AM transport. Both the canonical P-gp inhibitor CSA and microdevices (3000 microdevices/cm^2) inhibited P-gp as indicated by increased intracellular calcein concentrations (two-way ANOVA, Mean ± SD; ***p<0.0001; n=3). B) Caco-2 cells were grown on transwell membranes for 21 days prior to measurement of doxorubicin flux from the basolateral to apical compartments. The values shown are the cumulative amounts of doxorubicin transported into the apical chamber at each time (two-way ANOVA, Mean ± SD; ***p<0.0001; n=3). Doxorubicin flux was decreased by microdevices (3000 microdevices/cm^2) and CSA. Shown is one representative experiment of 3 independent experiments. C) R123 flux from the basal to apical chamber was measured in the presence and absence of microdevices and CSA. The values shown are the cumulative amounts of R123 measured in the apical chamber (two-way ANOVA, Mean ± SD; ***p<0.0001 w.r.t. untreated control; n=3). Microdevices and CSA both inhibited R123 flux and more inhibition of P-gp was seen with 3000 devices/cm^2 than 900 devices/cm^2. The two microdevice doses are significantly different at T=3 (*p<0.05) and T=4 (***p<0.0001). Shown is one representative experiment of 4 independent experiments. D) Recovery experiment with R123 where devices are removed, and transport into the apical chamber is measured over time. No difference is seen between the conditions once the devices are removed (two-way ANOVA, Mean ± SD; n=3).

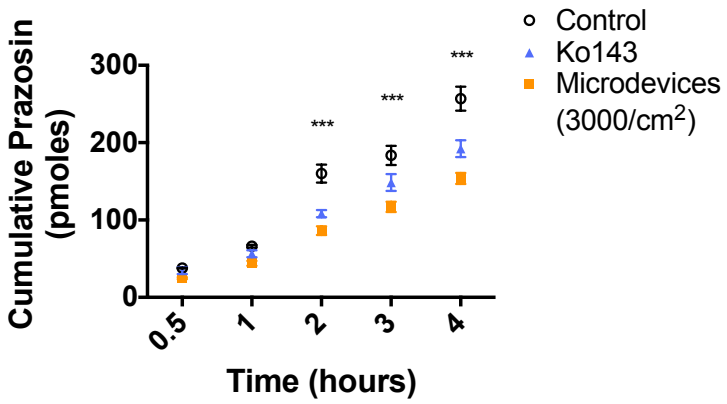

Figure 1.4: Microdevices inhibit BCRP transport in Caco-2 cells. Caco-2 cells were grown on transwell membranes for 21 days prior to measurement of prazosin transport. The values shown are the cumulative amounts of prazosin measured in the apical chamber (two-way ANOVA, Mean ± SD; ***p<0.0001 w.r.t. untreated control; n=3). Microdevices inhibit prazosin transport to a similar degree as CSA. Shown is one representative experiment of 3 independent experiments.

The P-gp and BCRP substrates used in these studies diffuse into the cells when placed on the basolateral side of Caco-2 cells. P-gp then actively transports R123 and doxorubicin while BCRP transports prazosin out of the cell into the apical compartment. Measurement from the basal to apical chamber allows for direct measurement of the function of the efflux transporters. Others have shown that there is minimal to no difference in the absence and presence of an inhibitor when these substrates are added to the apical side and detected on the basolateral side.[37–41] We see similar results with established P-gp and BCRP inhibitors, likely due to an insufficient change in the concentration gradient in the presence of inhibitor to detect concentration differences in the basolateral chamber.

Microdevices function through biosimilar mucus

The intestine has multiple barriers to prevent drug absorption, including the intestinal mucus. Although the mucus acts as a protective barrier to prevent bacterial microbes and toxic material from reaching the epithelial cells, it can also prevent drugs and drug delivery

formulations from interacting with these cells. A biosimilar mucus was used to test the effects of the microdevices in a transwell system.[34] The mucus was added to the apical chamber and allowed to incubate for 1 hour. Afterwards, the P-gp substrate R123 was added to the basal chamber and 3000 microdevices/cm^2 were added on top of the mucus layer. Similar to the experiments without mucus, microdevices inhibited P-gp as indicated by a decrease in R123 flux into the apical chamber; however, this inhibition of P-gp was delayed due to the need for the devices to permeate through the mucus for access to the transporter (Figure 1.5). While the effect of the microdevices on P-gp occurred within 2 hours without the mucus layer, inhibition was not detected until 4 hours after adding the microdevices with the mucus. Interestingly, the inhibitory effect of the microdevices was greater than that of CSA in the presence of mucus. This may be due to the small molecule being entrapped in the mucus and unable to interact with P-gp on the cell membrane. The microdevices were visible on the Caco-2 monolayer upon removal of the mucus layer. We hypothesis due to the weight and size of the microdevices that they are able to displace the mucus layer allowing them to travel through the mucus to interact with the membrane transporters on the cell surface. Compared to control, P_{app} decreases with microdevices to a similar extent as with CSA (Table 1.2). As the mucosal layer is a barrier to cell accessibility and drug absorption, the ability of the microdevices to penetrate this mucosal layer is critical for interaction with the intestinal cells to inhibit efflux transport.

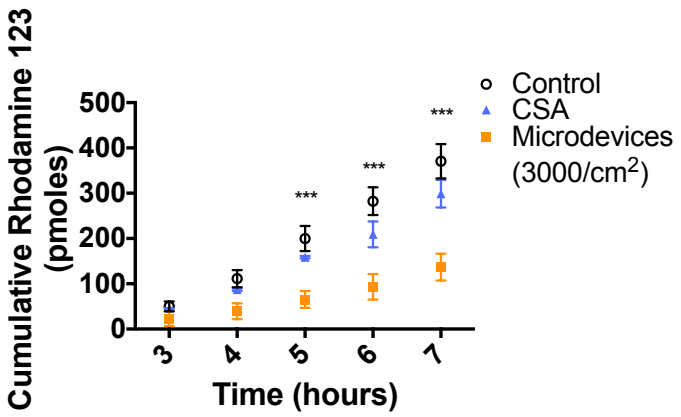

Figure 1.5: Microdevices inhibit P-gp transport through biosimilar mucus. Caco-2 cells were grown on transwell membranes for 21 days prior to measurement of R123 flux from the basal to apical chamber in the presence and absence of microdevices (3000 microdevices/cm^2) and CSA. The values shown are the cumulative amounts of R123 measured in the apical chamber at specific times (two-way ANOVA, Mean ± SD; ***$p<0.0001$ w.r.t. untreated control; n=3). Microdevices and CSA both inhibited R123 flux under conditions of a biosimilar mucus layer. Shown is one representative experiment of 3 independent experiments.

Microdevices affect P-gp function by decreasing cell surface expression

The possibility that the microdevices inhibit drug permeation by altering tight junctions was evaluated by measuring permeation of 4kDa FITC dextran. In the Caco-2 transwell system, the P_{app} for the 4kDa FITC dextran solution and the percentage that permeates the cell monolayer was unchanged with the addition of 3000 microdevices/cm^2 (4.7% permeation after 4 hours in the absence and presence of microdevices), indicating that the microdevices are not affecting paracellular drug transport (Figure 1.6A). To further test if the transport mechanism is active or passive, transport studies were performed at 4°C and 37°C. Inhibition of calcein AM transport with the microdevices was only apparent when the cells were kept at 37°C, indicating active transport is required for microdevice function (Figure 1.6B). In addition, we do not observe any changes in TEER with the microdevices present indicating the microdevices are not affecting paracellular drug permeation.

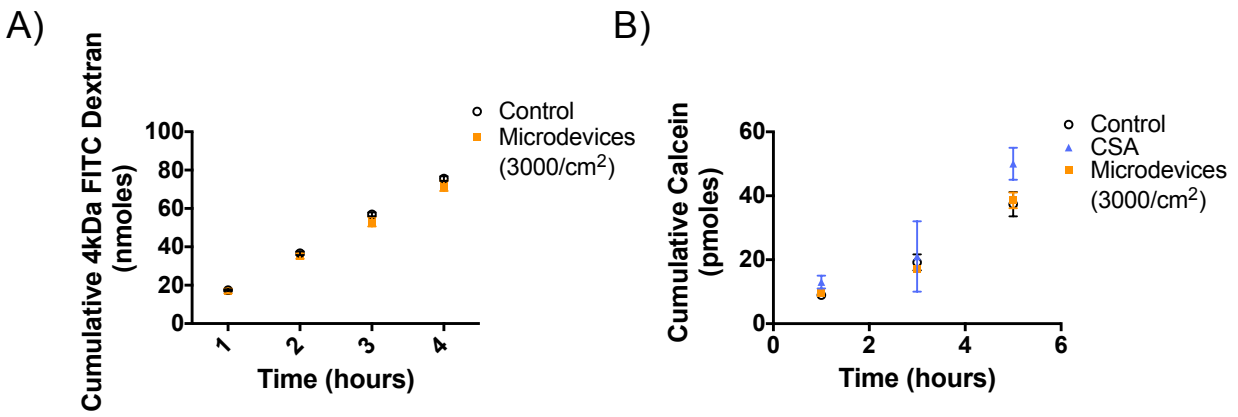

Figure 1.6: Microdevices do not affect passive permeability of Caco-2 cells. A) Caco-2 cells were grown on transwells for 21 days prior to measurement of apical to basal flux of 4 kDa FITC Dextran transport. The values shown are means ±SD of 3 biological replications. There was no effect of the microdevices on FITC dextran flux indicating no effect on tight junctions. B) Caco-2 cells were grown on 96 well plates for 14 days prior to measurement of intracellular calcein concentrations at 4°C. The values shown are means ±SD of 3 biological replications. There was no effect of the microdevices on calcein accumulation at 4ºC.

The effect of the microdevices on P-gp expression was also considered. To test whether the microdevices were affecting transporter expression levels on the mRNA level, qPCR was performed. P-gp and BCRP mRNA levels remain unaltered after 3 hours of treatment with the microdevices compared to control (Figure 1.7A). Due to the short time scale of hours in the microdevice treatment, a change in mRNA levels is not necessarily expected. To further test if a direct change in cell surface P-gp protein amounts were altered in the presence of the microdevices we performed flow cytometry. Briefly, Caco-2 cells grown on transwells were exposed to microdevices for 3 hours, stained with a P-gp antibody that recognizes an external epitope, and analyzed by flow cytometry. Exposure to the microdevices caused a decrease in levels of P-gp on the cell membrane when compared to untreated cells (Figure 1.7B). We propose that the decrease in cell surface P-gp is due to the interactions with the microdevices, which then leads to decreased P-gp function. The structure of P-gp in the transmembrane domain has been shown to be tightly integrated with cholesterol and phospholipids, and this interaction is

critical for transporter dynamics.[42] Whether the microdevices affect P-gp function by disrupting these interactions requires investigation. Consistent with previous work, altering the cell surface interactions of the transporter can indeed affect transporter function.[43] Additionally, it is plausible that the microdevices sterically hinder the conformational changes required for P-gp to release a substrate from the binding site in the transmembrane region to the apical chamber, resulting in P-gp inhibition. Such steric hinderance could also lead to internalization of the transporter as supported by the decrease membrane expression after exposure to microdevices (Figure 1.7B).

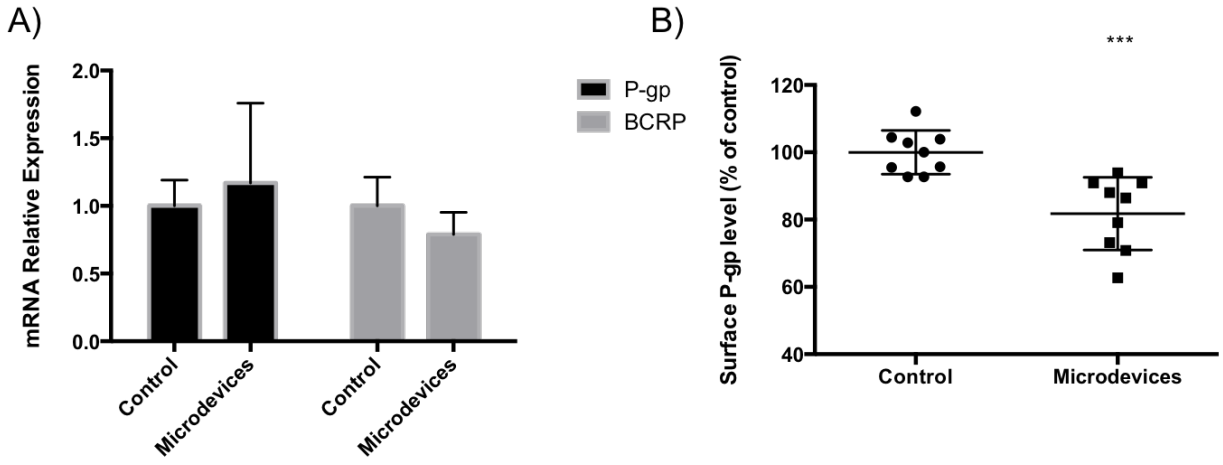

Figure 1.7: Microdevices decrease cell surface P-gp levels in Caco-2 cells. Caco-2 cells were grown on transwells for 21 days and A) mRNA levels corresponding to P-gp (ABCB1) and BCRP (ABCG2) in the absence and presence of microdevice exposure for 3 hours were measured by qPCR. B) Following the same treatment of Caco-2 cells with microdevices, cell surface P-gp levels were analyzed by flow cytometry. P-gp levels are expressed relative to levels in cells without microdevices (two-tailed t-test, Mean ± SD; ***$p<0.0001$; n=9). Surface P-gp protein levels were decreased in cells after addition of the microdevices.

Ex vivo mouse model to measure R123 transport

Ex vivo models allow for increased complexity of intestinal epithelium interactions over 2D culture methods while allowing for higher throughput over *in vivo* studies.[44] We isolated and sectioned the mouse jejunum into 4 cm regions to generate intestinal sacs. The intestinal sacs

were loaded with R123 in the absence or presence of 3000 microdevices/cm^2 or CSA on the mucosal side. The intestine was closed on both sides and transport of R123 across the intestinal barrier of the epithelial cells was measured on the serosal side. We showed a significant increase in transport of R123 to the serosal side in the presence of microdevices compared to control (Figure 1.8). The P_{app} increases in the presence of microdevices compared to control. This suggests that the microdevices were able to inhibit P-gp in a physiological *ex vivo* model, increasing drug transport across the cell to the serosal side. This *ex vivo* model better represents an *in vivo* oral dose where the drug substrate is interacting with the epithelial cells on the mucosal side to increase drug absorption to the serosal side.

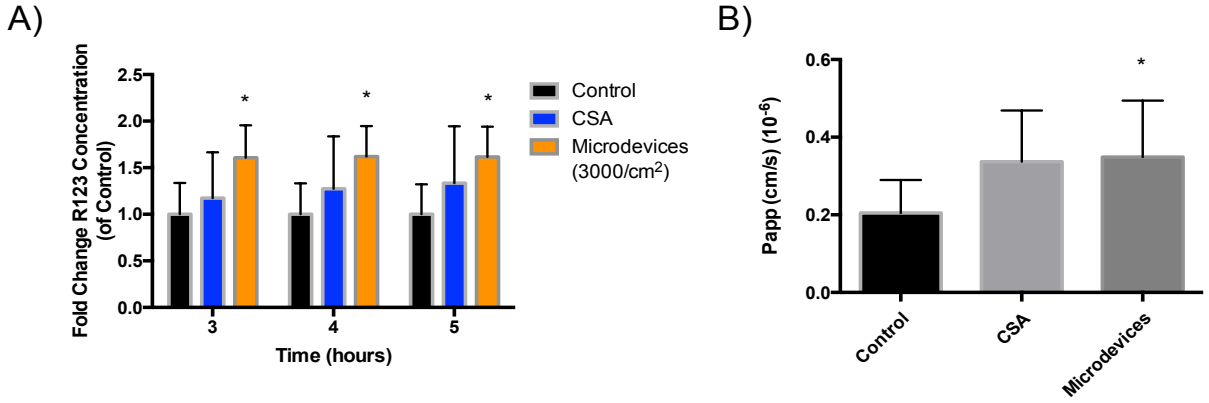

Figure 1.8: **Microdevices increase mucosal to serosal transport of R123 in an *ex vivo* mouse model.** Jejunum was sectioned to form intestinal sacs where R123 transport was measured over time in the presence and absence of microdevices (3000 microdevices/cm^2) or CSA. A) Fold change of R123 transport compared to control, without microdevices. (Two-way ANOVA, Mean ± SD; *p<0.05 w.r.t. untreated control, n=6 Control, n=4 CSA, n=6 Microdevices) B) Calculated P_{app} of R123 transport with an increase in P_{app} from 0.2*10^{-6} cm/sec (control) to 0.35*10^{-6} cm/sec with microdevices and 0.33*10^{-6} cm/sec with CSA. R123 transport from mucosal to serosal side was increased with microdevices. (Two-tailed t-test, Mean ± SD;* p<0.05 w.r.t. untreated control, n=6 Control, n=4 CSA, n=6 Microdevices)

In vivo mouse model to measure R123 Transport

In vivo mouse models represent a more physiological environment where mucus, microbiome, and peristalsis flow which are difficult to represent *in vitro* are intact. Microdevices (400,000 microdevices/kg total dose), or CSA were given by gavage to C57BL/6 mice after a 12-

hour fasting period. Microdevices were preincubated for 2 hours while CSA was preincubated for 30 minutes, then R123 was given by oral gavage to the mice. Blood was collected over time through a submandibular vein. A significant increase in R123 C_{max} was measured with CSA and microdevices compared to control (Figure 1.9). The C_{max} and $AUC_{0\text{-}60min}$ increase is consistent with changes in the absorption phase of R123. Previous studies in rodents demonstrated rapid systemic hydrolysis of R123 to the corresponding acid, R110.[45,46] Since the fluorescence assay used to detect R123 will also detect R110, it is difficult to interpret potential effects on the elimination phase of R123, although inhibition of P-gp in the liver or kidney is not expected since the microdevices are too large to be absorbed. This suggests that microdevices are able to inhibit P-gp *in vivo,* even with multiple barriers in the stomach and intestine, leading to increased R123 absorbed into systemic circulation.

A)

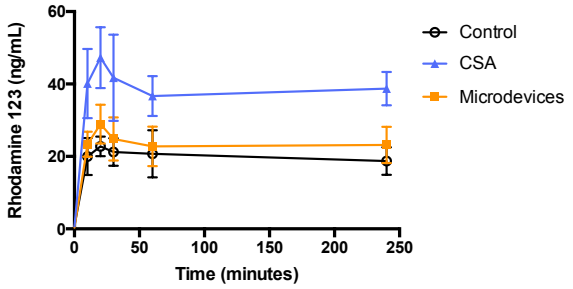

B)

	Control	CSA	Microdevices
C_{max} (ng ml^{-1})	22.78 ± 2.7	38.7 ± 4.6	28.92 ± 5.4
$AUC_{0\text{-}60min}$ (ng ml^{-1} h)	19.39 ± 3.5	37.5± 5.9	22.61 ± 4.2

Figure 1.9: **Microdevices increase systemic circulation of R123 in an *in vivo* mouse model.** Oral gavage of microdevices (400,000 devices/kg), CSA, and R123 was performed on C57BL/6 mice where R123 transport was measured over time. A) Systemic R123 amounts measured in serum over time B) C_{max} and $AUC_{0\text{-}60min}$ values analyzed from the concentration-time curve (two-tailed t-test, Mean ± SD; C_{max} p=0.012 Control vs Microdevices; n=8 Control, n=5 CSA, n=8 Microdevices)

Table 1.2. P_{app} values of P-gp and BCRP substrates

P_{app} (cm/s) (10^{-6})	Control	Inhibitor	Microdevices
R123	8.03 ± 3.5	2.03 ± 0.71	5.51 ± 2.4
Doxorubicin	1.90 ± 0.35	1.33 ± 0.46	1.74 ± 0.25
Prazosin	10.18 ± 0.25	8.21 ± 0.90	7.36 ± 1.7
R123 with mucus	9.25 ± 3.8	3.53 ± 3.5	4.21 ± 0.51

P_{app} was calculated in 3-4 independent experiments and the mean ±SD are represented in the table.

Conclusions

The importance of gut efflux transporters in limiting drug absorption is well recognized. Attempts at inhibiting efflux transporters as a strategy to improve bioavailability have been limited by adverse events.[15] Thus, there is a critical need for novel strategies to inhibit efflux transporters to improve oral drug absorption, particularly for drug substrates such as chemotherapeutics and immunosuppressants. Here, a materials-based approach was applied to study the effects of biocompatible crosslinked PEGDMA materials and their effects on efflux transporters. Due to the frequent use of PEG based materials in oral drug delivery, it is important to better understand the cellular-level effects of these materials as they interact with the intestinal epithelium. Here we demonstrated that PEGDMA microdevices inhibit P-gp and BCRP in a transwell Caco-2 model. The inhibition of P-gp was dose dependent with a greater number of microdevices resulting in increased P-gp inhibition. Dose dependence allows for control of the degree of inhibition based on drug or patient characteristics. In addition, the P-gp inhibition was completely reversible upon the removal of the microdevices. Importantly, the microdevices can

function as P-gp inhibitors through a biosimilar mucus *in vitro* and increase mucosal to serosal drug transport in an *ex vivo* mouse intestinal sac model. Furthermore, in an *in vivo* mouse model, the microdevices increase C_{max} and $AUC_{0\text{-}60min}$ of R123 compared to control, indicating the microdevices are acting as P-gp inhibitors *in vivo*. The decrease in P-gp function is likely due at least in part to a reduction in P-gp on the cell membrane in the presence of the microdevices.

Since the microdevices only interact with the surface of the intestinal cell and do not enter systemic circulation, our approach presents a nonpharmacological method to inhibit P-gp with the goal to limit toxicity and adverse effects from current small molecule inhibitors. These findings open new possibilities for oral P-gp inhibition with the potential to locally and reversibly inhibit P-gp using microdevices. A more extensive characterization of the mechanism by which microdevices inhibit P-gp is required to fully understand their interaction with gut P-gp and to support novel therapeutic approaches to improve oral drug bioavailability. While a representative fluorescent P-gp substrate, R123, was used as a model substrate, this system can be translated to drugs that have limited oral bioavailability due to P-gp efflux. Moreover, the knowledge gained in this study will be broadly useful in the design of hydrogel-based oral delivery systems, particularly with drugs that are efflux transporter substrates.

References

1. Sastry, S., Nyshadham, J. & Fix, J. Recent technological advances in oral drug delivery - a review. *Pharm. Sci. Technolo. Today* **3,** 138–145 (2000).

2. Gupta, H., Bhandari, D. & Sharma, A. Recent trends in oral drug delivery: a review. *Recent Pat. Drug Deliv. Formul.* **3,** 162–173 (2009).

3. Verma, R. K., Mishra, B. & Garg, S. Drug Development and Industrial Pharmacy Osmotically Controlled Oral Drug Delivery. *Drug Dev. Ind. Pharm.* **267,** 695–708 (2000).

4. Ensign, L. M., Cone, R. & Hanes, J. Oral drug delivery with polymeric nanoparticles: The gastrointestinal mucus barriers. *Adv. Drug Deliv. Rev.* **64,** 557–570 (2012).

5. Goldberg, M. & Gomez-Orellana, I. Challenges for the oral delivery of macromolecules. *Nat. Rev. Drug Discov.* **2,** 289–95 (2003).

6. Chan, L. M. S., Lowes, S. & Hirst, B. H. The ABCs of drug transport in intestine and liver: efflux proteins limiting drug absorption and bioavailability. *Eur. J. Pharm. Sci.* **21,** 25–51 (2004).

7. Amin, M. L. P-glycoprotein Inhibition for Optimal Drug Delivery. *Drug Target Insights* **7,** 27–34 (2013).

8. Lin, J. H. & Yamazaki, M. Role of P-Glycoprotein in Pharmacokinetics. *Clin. Pharmacokinet.* **42,** 59–98 (2003).

9. Lomovskaya, O. & Bostian, K. A. Practical applications and feasibility of efflux pump inhibitors in the clinic—A vision for applied use. *Biochem Pharmacol.* **71:7,** 910-8 (2006)

10. Giacomini, K. M. *et al.* Membrane transporters in drug development. *Nat. Rev. Drug Discov.* **9,** 215–236 (2010).

11. International Transporter Consortium, T. I. T. *et al.* Membrane transporters in drug

development. *Nat. Rev. Drug Discov.* **9,** 215–36 (2010).

12. Karolewicz, B. A review of polymers as multifunctional excipients in drug dosage form technology. *Saudi Pharm. J.* **24,** 525–536 (2016).

13. Varma, M. V. S., Ashokraj, Y., Dey, C. S. & Panchagnula, R. P-glycoprotein inhibitors and their screening : a perspective from bioavailability enhancement. **48,** 347–359 (2003).

14. Robert, J., Jarry, C. Multidrug Resistance Reversal Agents. *J. Med. Chem.* **46:23,** 4805-4817 (2003).

15. Raghava, K. M. & Lakshmi, P. K. Overview of P-glycoprotein inhibitors: A rational outlook. *Brazilian J. Pharm. Sci.* **48,** 353–367 (2012).

16. W. Robey, R., R. Massey, P., Amiri-Kordestani, L. & E. Bates, S. ABC Transporters: Unvalidated Therapeutic Targets in Cancer and the CNS. *Anticancer. Agents Med. Chem.* **10,** 625–633 (2011).

17. Tamaki, A., Ierano, C., Szakacs, G., Robey, R. W. & Bates, S. E. The controversial role of ABC transporters in clinical oncology. *Essays Biochem.* **50,** 209–232 (2011).

18. Yuan, Y. *et al.* Nanoparticle delivery of anticancer drugs overcomes multidrug resistance in breast cancer. *Drug Deliv.* **23,** 3350–3357 (2016).

19. Kam, K. R. *et al.* Nanostructure-mediated transport of biologics across epithelial tissue: Enhancing permeability via nanotopography. *Nano Lett.* **13,** 164–171 (2013).

20. Fox, C. B. *et al.* Fabrication of Sealed Nanostraw Microdevices for Oral Drug Delivery. doi:10.1021/acsnano.6b00809

21. Gupta, P., Vermani, K. & Garg, S. Hydrogels: From controlled release to pH-responsive drug delivery. *Drug Discovery Today* (2002). doi:10.1016/S1359-6446(02)02255-9

22. Sharpe, L. A., Daily, A. M., Horava, S. D. & Peppas, N. A. Therapeutic applications of

hydrogels in oral drug delivery. *Expert Opin. Drug Deliv.* **11,** 901–15 (2014).

23. Puranik, A. S., Pao, L. P., White, V. M. & Peppas, N. A. In Vitro Evaluation of pH-Responsive Nanoscale Hydrogels for the Oral Delivery of Hydrophobic Therapeutics. *Ind. Eng. Chem. Res.* **55,** 10576–10590 (2016).

24. Horava, S. D., Moy, K. J. & Peppas, N. A. Biodegradable hydrophilic carriers for the oral delivery of hematological factor IX for hemophilia B treatment. *Int. J. Pharm.* **514,** 220–228 (2016).

25. Culver, H. R. *et al.* HHS Public Access. **50,** 170–178 (2018).

26. Dash, A. K. & Ii, G. C. C. Therapeutic Applications of Implantable Drug Delivery Systems. **12,** 1–12 (1999).

27. Larrañeta, E., Stewart, S., Ervine, M., Al-Kasasbeh, R. & Donnelly, R. F. Hydrogels for hydrophobic drug delivery. Classification, synthesis and applications. *J. Funct. Biomater.* **9,** (2018).

28. Lin, C. C. & Anseth, K. S. PEG hydrogels for the controlled release of biomolecules in regenerative medicine. *Pharm. Res.* **26,** 631–643 (2009).

29. Hugger, E. D., Audus, K. L. & Borchardt, R. T. Effects of poly(ethylene glycol) on efflux transporter activity in Caco-2 cell monolayers. *J. Pharm. Sci.* **91,** 1980–1990 (2002).

30. Hodaei, D., Baradaran, B., Valizadeh, H. & Zakeri-milani, P. Effects of polyethylene glycols on intestinal efflux pump expression and activity in Caco-2 cells. *Braz. J. Pharm. Sci.* **51,** (2015).

31. Shen, Q. *et al.* Modulation of intestinal P-glycoprotein function by polyethylene glycols and their derivatives by in vitro transport and in situ absorption studies. *Int. J. Pharm.* **313,** 49–56 (2006).

32. Chirra, H. D. *et al.* Planar Microdevices for Enhanced In Vivo Retention and Oral Bioavailability of Poorly Permeable Drugs. *Adv. Healthc. Mater.* **3,** 1648–1654 (2014).

33. Le, L. V. *et al.* Injectable hyaluronic acid based microrods provide local micromechanical and biochemical cues to attenuate cardiac fibrosis after myocardial infarction. *Biomaterials* **169,** 11–21 (2018).

34. Boegh, M., Baldursdóttir, S. G., Müllertz, A. & Nielsen, H. M. Property profiling of biosimilar mucus in a novel mucus-containing in vitro model for assessment of intestinal drug absorption. *Eur. J. Pharm. Biopharm.* **87,** 227–235 (2014).

35. Kowapradit, J. *et al.* In vitro Permeability Enhancement in Intestinal Epithelial Cells (Caco-2) Monolayer of Water Soluble Quaternary Ammonium Chitosan Derivatives. *AAPS PharmSciTech* **11,** 497–508 (2010).

36. DeVries, N. A. *et al.* P-glycoprotein and breast cancer resistance protein: Two dominant transporters working together in limiting the brain penetration of topotecan. *Clin. Cancer Res.* **13,** 6440–6449 (2007).

37. Stormer, E., et al. Methadone Inhibits Rhodamine123 Transport in Caco-2 Cells. *Drug Metab. Dispos.* **30,** 483–487 (2002).

38. Chimezie, C. *et al.* Glyceollin Transport, Metabolism, and Effects on P-Glycoprotein Function in Caco-2 Cells. *J. Med. Food*. **17,** 462–471 (2014).

39. Sugihara, N. *et al.* Effect of benzo [a] pyrene on P-glycoprotein-mediated transport in Caco-2 cell monolayer. *Toxicology*. **223,** 156–165 (2006).

40. Li, Y. *et al.* Phorbol 12-myristate 13-acetate inhibits P-glycoprotein-mediated efflux of digoxin in MDCKII- MDR1 and Caco-2 cell monolayer models. *Nat. Publ. Gr.* **35,** 283–291 (2013).

41. Oga, E. F., Sekine, S., Shitara, Y. & Horie, T. Potential P-Glycoprotein-Mediated Drug-Drug Interactions of Antimalarial Agents in Caco-2 cells. *Am. J. Trop. Med. Hyg.* **87,** 64–69 (2012).

42. Alam, A., Kowal, J., Broude, E., Roninson, I. & Locher, K. P. Structural insight into substrate and inhibitor discrimination by human P-glycoprotein. *Science.* **363,** 753–756 (2019).

43. Dai, Z., Yao, Q. & Zhu, L. MMP2-Sensitive PEG-Lipid Copolymers: A New Type of Tumor-Targeted P-Glycoprotein Inhibitor. *ACS Appl. Mater. Interfaces* **8,** 12661–12673 (2016).

44. Goggin, B. J. *et al.* Intestinal Sacs to Assess Mucosal Permeability in Models of Gastrointestinal Disease. *J. Vis. Exp.* **199,** 1–7 (2016).

45. Zhao, W. *et al.* Effects of Polyoxyethylene Alkyl Ethers on the Intestinal Transport and Absorption of Rhodamine 123: A P-glycoprotein Substrate by in Vitro and in Vivo Studies. *J. Pharm. Sci.* **105,** 1526–1534 (2016).

46. Forster, S., Thumser, A. E., Hood, S. R. & Plant, N. Characterization of rhodamine-123 as a tracer dye for use in in vitro drug transport assays. *PLoS One* **7,** (2012).

CHAPTER 2: Innate Activating Nanoparticles Lead to Activation of Antigen Presenting Cells to Reduce Tumor Burden

Abstract

Cancer immunotherapy has been a growing field based on exciting clinical results that have improved patient outcome. Even with the ongoing trials further investigating the benefits of activating the immune system there still are limitations due to toxicity, nonspecificity, and high dose requirements for therapeutic efficacy. Here, we show that with a nanomaterials approach combined with an adjuvant cocktail including a TLR9 agonist, STING agonist, and RIG-I agonist along with a melanoma specific peptide, decreased the tumor presence in a subcutaneous and metastasis model. These innate activating nanoparticles (iaNPs) internalize and activate antigen presenting cells downstream leading to the promotion of melanoma sensitized T cells. This combination adjuvant cocktail and biomaterials-based approach to activate the innate immune response provides further insight to the benefits of stimulating multiple activation pathways to promote tumor regression.

Introduction

Due to the failure of current highly invasive treatments for cancer with traditional chemotherapy and radiotherapy, there is an urgent need for new therapeutic developments to improve outcomes and patient compliance. Oncolytic viruses have been studied to effectively promote anti-tumor response and immunity.[1,2] Strategies involving oncolytic therapy are promising and multiple clinical trials are ongoing.[3–5] Oncolytic therapy involves multiple different pathways resulting in the lysis of tumor cells and release of antigens, cytokines and pathogen-associated molecular patterns (PAMPs) which all promote the activation of antigen-presenting cells (APCs).[1,6] Downstream these APCs lead to promotion of tumor antigen specific CD4 and CD8 T cells which promotes tumor regression and death.[7–9] Activated CD8 T cells release cytokines, and cause granule exocytosis and Fas ligand-mediated apoptosis to exert antitumoral effects.[10] Similar to CD8 T cells, CD4 T cells can mediate tumor death through direct interactions with tumor cells through release of cytokines and Fas mediated pathway.[11] Additionally, CD4 T cells can also indirectly kill tumor cells through helper functions, improving the efficacy of tumor reactive CD8 T cells.[9,12,13] The PAMPs pathway involves a variety of different mechanisms that could lead to APC stimulation and downstream activation of the JAK-STAT pathway to trigger local interferon (IFN) release. For example, PAMPs can induce Toll-like-receptor (TLR) binding and activation, stimulator of interferon genes (STING), and retinoic acid inducible gene 1 (RIG-I).[2,6,14] As a result, we wanted to develop a potent system based off the oncolytic virus to activate TLR9, STING, and RIG-I pathways in tumors (Figure 2.1).

CpG-ODN 1826 has been studied as a TLR9 agonist to treat cardiac dysfunction and cancer.[15–17] TLR9 recognizes unmethylated CpG dinucleotides which are found in viral and

bacterial DNA.[18] In a cell's resting state, TLR9 is found in the endoplasmic reticulum but in the presence of CpG ODN the TLR9 colocalizes with the CpG ODN in the endosomal compartment resulting in binding and pathway activation.[19] Upon binding to CpG ODN, TLR9 stimulation leads to activation of the Th1 pathway which can directly lyse infected cells by natural killer (NK) and cytotoxic T lymphocyte (CTL) activation.[16,20] TLR9 stimulation also activates plasmocytoid dendritic cells (pDCs) to secrete type I interferons and to increase activation of B cells and pDCs which leads to T cell activation and an immune response (Figure 2.1). Overall TLR9 pathway activation can lead to tumor cell death directly through production of factors such as IFNα or indirectly though NK activation. As a result, to modulate the innate and downstream adaptive immune system, we included the CpG-ODN1826 TLR9 agonist in our adjuvant cocktail.

To activate the STING pathway, we investigated the STING agonist 3'3 cGAMP. STING is a transmembrane protein that is found on many APCs such as macrophages and dendritic cells.[21] Pathogens produce cytosolic cyclic di-nucleotides (CDNs) which are recognized by STING and lead to pathway activation. The binding of 3'3 cGAMP with STING leads to signaling events resulting in an increase in IFNβ expression (Figure 2.1).[22–24] Similar to the STING activation, RIG-I activation induces the secretion of proinflammatory cytokines such as type I interferon alpha and beta.[25] RIG-I is a cytosolic protein that recognizes viral RNA evoking the innate immune response. 5'pppdsRNA is an agonist to RIG-I, and once bound to the RIG-I receptor, RIG-I undergoes an ATP dependent conformational change exposing the caspase recruitment domain (CARD).[26] Upon exposure of CARD domain, this leads to downstream signaling and active production of type I interferons (Figure 2.1). Interferons have been shown to upregulate MHC I and MHC II promoting APC activation along with promoting apoptosis of

tumor cells through the JAK/STAT pathway.[27–29] Although RIG-I receptor targets RNA while STING receptor targets DNA, there is cross-talk between these pathways which can lead to amplification of the innate immune system.[30]

In addition to the RIG-I, STING, and TLR9 agonists, we combine a TRP-2 or gp100 peptide which is specific for melanoma cells. TRP-2 and gp100 proteins are overexpressed on the surface of melanoma cells.[31] Stimulation of the innate immune system with proinflammatory cytokine production and DC activation leads to downstream activation of the adaptive immune system by generation of TRP-2 or gp100 specific CD4 and CD8 T cells to target and reduce melanoma tumor burden (Figure 2.1).[32–34] Tumor specific antigen therapeutics have developed into a promising therapy especially as a combination therapy with multiple current clinical studies (clinicaltrials.gov NCT04024800, NCT02754362).[35] Generation of these antigen specific T cells allows for targeting of the cytotoxic T cells to the tumor to induce tumor cell death.

Even though these therapeutics have shown promise to mechanistically reduce tumor burden, a limiting factor to achieve optimal therapeutic effect and tumor burden is exposure. Small molecule and protein therapeutics are cleared rapidly from systemic circulation and lack sufficient uptake into cellular targets, resulting in limited therapeutic effects.[36,37] As a result, the development of a nanoscale system to efficiently protect the therapeutics from degradation, increase the systemic half-life, and efficiently internalize into the target cells has improved cancer immunotherapy formulations.[38] Various nano-based carrier formulations have shown promising efficacy to deliver proteins and small molecules including polymer nanoparticles, liposomes, and hydrogels. [39–43]

With the aim to develop a therapeutic to address the challenges discussed above, we construct an innate activating nanoparticle (iaNP) composed of a biodegradable polymer loaded

with a potent combination of a TLR9 agonist, RIG-I agonist, STING agonist, and a melanoma specific peptide (TRP-2 or gp100). With this adjuvant combination we hypothesize that the iaNP would activate the innate immune system to increase APC presentation and downstream lead to activation of tumor sensitized T cells to target and kill tumor cells. We investigated and characterized the response of APC in the presence of iaNP *in vitro* and *in vivo* and the tumor efficacy response *in vivo* in both a melanoma subQ and metastasis model.

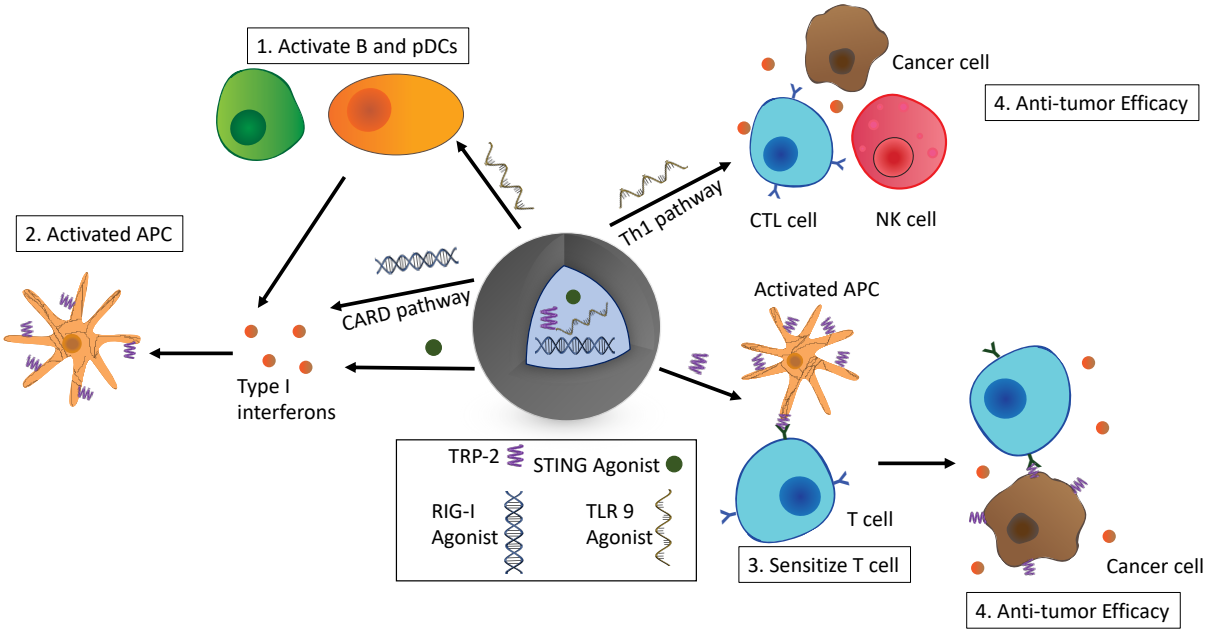

Figure 2.1: Anti-tumor pathways activated with iaNPs. iaNP were loaded with STING, RIG-I, and TLR9 agonist along with cancer cell specific peptide, TRP-2. (1) TLR9 agonist activated B and pDCs leading to type I interferon production and activation of APCs. (2) RIG-I and STING agonist promote type I interferon production and activation of APCs. (3) Activated APCs present the TRP-2 peptide on the surface leading to sensitizing T cells to generate TRP-2 specific T cells. (4) TRP-2 specific T cells can then target cancer cells that express the TRP-2 protein on the surface leading to anti-tumor efficacy. (5) TLR 9 agonist also leads to anti-tumor efficacy through the Th1 pathway and activation of CTL and NK cells to directly kill cancer cells.

Materials & Methods

Nanoparticle fabrication

Nanoparticles (NPs) composed of carboxylic acid terminated poly (lactic-co-glycolic acid (PLGA) (PolySciTech) were made by double emulsion probe sonication. 1200 mg of 75:25 lactic:glycotic (L:G) PLGA was dissolved in ethyl acetate (Sigma) at 50 mg/mL. CpG ODN 1826 (TLR9 agonist, 75 µg, Trilink), 5'ppp-dsRNA (RIG-I agonist, 15µg, Invivogen), 3'3-cGAMP (STING agonist, 150µg, Invivogen), and a melanoma peptide (TRP-2 or gp100, 2mg, Sigma) were solubilized in aqueous Limulus amebocyte lysate (LAL) water. Polyvinyl alcohol (PVA, Sigma) at 3% (w/v) was added at a 1:2 ratio of polymer drug solution to PVA. The mixture was probe sonicated on ice at 7-8 W which is equal to 30 amplitude for 5 cycles of 5 second on and 10 seconds off to form NPs. The NP solution was diluted 10-fold with 0.3% (w/v) PVA and slowly stirred for 2 hours to evaporate the ethyl acetate. The NPs were purified first to remove large aggregates by centrifuging at 500 rpm for 10 minutes. Then to remove small NPs and unencapsulated drug, the NP solution was centrifuged at 13,000 rpm for 10 minutes. The NPs were lyophilized and stored at -80C. Prior to *in vitro* and *in vivo* work, the NPs were resuspended in 1% PVA in Phosphate Buffer Saline (PBS).

Total drug payload

Drug Loading was determined by Size Exclusion Chromatography (SEC). Mobile Phase was 0.05M Potassium Phosphate Buffer with 0.25M Potassium Chloride, pH 6.8 which was run at a flow rate of 0.35 ml/min over 20 minutes. Adjuvant loading was determined over time until total payload was released out of the nanoparticles in PBS. Rention times for the adjuvants were 6.5 minutes for CpG ODN 1826, 5.9 minutes for 5'ppp-dsRNA, 7.5 minutes for 3'3-cGAMP, 11.9 minutes for the TRP-2 peptide.

Mice and cell culture

The mouse studies were performed in compliance with the University of California, San Francisco Institutional Animal Care and Use Committee guidelines with the approved Protocol AN110246. Wild type C57BL/6 mice were 6-8 weeks purchased from The Jackson Laboratory. Cell culture was performed with complete media containing RPMI 1640 with 10% Calf Serum (heat inactivated, Sigma), 1% Penicillin Streptomycin (Sigma), 1 mM Sodium Pyruvate (Sigma), 1% HEPES (Sigma), 1x non-essential amino acids (Sigma), 50 μM of 2-beta mercaptoethanol (Sigma). B16-F10 melanoma cells (ATCC) were cultured in a T-75 flask until 70% confluency prior to injection. For IV melanoma administration, the cells were removed from the flask, washed with ice-cold Hank's Balanced Salt Solution (HBSS) (Thermo), and filtered prior to mouse tail vein injection of $2.5*10^6$ cells/mouse.[44] Cells were maintained in a humidified incubator at 37°C with 5% CO_2. J774.1 macrophages (ATCC) confocal experiments were performed with nanoparticles with a fluorescent polymer Cyano-Polyphenylene vinylene (CN-PPV) (Sigma) incorporated to track the nanoparticles. Macrophages were activated overnight with Lipopolysaccharide (LPS) (10 ng/mL, Sigma) and cultured with nanoparticles for 3 hours prior to washing and imaging.

***In vitro* nanoparticle uptake and activation experiments**

Spleen was harvested from mice. Spleen was extracted and mashed through a 70 μm filter with PBS. Splenocytes were centrifuged down at 1500 rpm for 5 minutes. The pellet was resuspended into RBC lysis (0.83% ammonium chloride in 0.01 M Tris buffer) for 5 minutes at 37C. Cells were washed 2 x with complete media. $1*10^6$ cells were placed in 96 wells.
For nanoparticle uptake experiments, cells were cultured with NPs with a CN-PPV fluorescent polymer incorporated for tracking for 48 hours. Excess nanoparticles were washed 3x with

Phosphate Buffer Saline (PBS) (Sigma) with 4% fetal bovine serum (FBS) (Sigma). Cells were stained for flow cytometry.

For APC activation experiments, cells were treated with iaNP, NP only, and control no treatment. After 48 hours the cells were stained with antibodies and run on flow cytometry.

Subcutaneous *in vivo* melanoma model

Female C57BL/6 mice aged 6-8 weeks from Jackson Laboratory were inoculated with $1*10^5$ B16F10 cells in PBS buffer. Mice were treated with saline, NP only, iaNP, free unencapsulated drug 3 days after tumor inoculation every 3 days for a total of 4 doses. Intratumoral treatment was injected in 4 separate spots in the tumor for a total of 100 µL. For intravenous treatment, 200 µL of treatment was injected tail-vein. A caliper was used twice a week for tumor measurements.

Intravenous *in vivo* melanoma model

B16F10 melanoma was added IV to C57BL/6 mice. After 4 days treatment was administered either PVA only, NP only, or iaNP IV to the melanoma treated mice. Treatment was administered 3 times every 3 days. 3 days after the last treatment, the mice were sacrificed and the spleen, lymph nodes, and lungs were harvested. The number of lung foci and weight was measured upon removal prior to digestion. The spleen and lymph nodes were passed through 100 µm filter. RBC lysis was performed on splenocytes. Lung was finely minced and digested in media containing collagenase XI (2 mg/mL, Sigma Aldrich), DNAse (0.1 mg/mL, Sigma Aldrich), and hyaluronidase (0.5 mg/mL, Sigma Aldrich) at 200 rpm and 37°C for 45 minutes. The lung suspension was diluted 10-fold with media, vortexed to disturb the pellet and passed through a 100 µm filter. After forming single cell suspensions, the lymph node, splenocytes, and lung cells were plated in a 96 well plate.

Protein Transport Inhibitor (GolgiPlug, BD) at 1uL/mL was added to single cell suspensions. Cells were then stimulated with 10 μg/mL of TRP-2 in culture for 12 hours. The cells were stained for flow cytometry.

In vivo dendritic cell activation was measured 5 days after 1 dose of iaNP, NP only, or control no treatment. The mice were sacrificed and single cell cultures of the spleen, lymph node, and lungs were generated as described above. The cells were then stained for flow cytometry.

Flow cytometry analysis and panels

For flow cytometry experiments single cells are plated in 96 wells plates at 1-2 *10^6.The plate in centrifuged down at 2,000 rpm for 2 minutes twice with PBS+2% FBS. The cells were resuspended in 50 μL of surface antibody mixture and incubated at 4°C for 30 minutes. After 30 minutes, the surface antibody was washed 2x with PBS with 2% FBS. Cells were resuspended in 50 μL of Fix/Perm (1:4) for 30 minutes. Wells were washed twice with Perm Buffer at 2000 rpm for 4 minutes. The cells were then incubated with intracellular antibody stain for 30 minutes at 4C. Cells were washed 2x with PBS 2% FBS and resuspended and stored in PBS FBS at 4°C. Flow cytometry was performed on Fortessa X-20 and data analysis was performed with FlowJo For cell uptake experiments the surface antibody stain contains anti-CD3-FITC, anti-CD11c-PECy7, anti-CD11b-BV650, anti-CD45-Alexa700, anti-CD64-BV786, anti-B220-APCCy7, anti-CD19-PE, Ghost Violet 510 viability dye (Tonbo). Nanoparticles with the CN-PPV incorporated polymer were analyzed in the PerCP channel.

For APC activation *in vitro* and *in vivo*, a dendritic cell and a macrophage panel were studied. Surface antibody stain for the DC panel were anti-CD3-PerCP, anti-CD11c-PE-Cy7, anti-CD11b-BV650, anti-CD45-Alexa700, anti-MHCII-e450, anti-Ly6C-BV605, anti-CD86-APC, anti-B220-APC-Cy7, anti-CD207-PE, and Ghost Violet 510 viability dye (Tonbo).

Surface antibody stain for the macrophage panel were anti-B220-FITC, anti-CD19-FITC, anti-CD3-FITC, anti-CD11c-PECy7, anti-CD11b-BV650, anti-CD45-Alexa700, anti-MHCII-e450, anti-CD64-BV786, anti-CD24-APC eFluor-780, and Ghost Violet 510 viability dye.

Macrophage intracellular antibody stain mix contained anti-IL10-APC and anti-IL12-PE. TRP-2 stimulation surface antibody panel was anti-CD45.2-FITC, anti-CD8-BV605, anti-CD45-Alexa700, anti-CD4-BV650, anti-CD3e-BV711, anti-FOXP3-e450, and Ghost Violet 510 viability dye. The stimulation intracellular antibody stain contained anti-Ki67-PECy7, anti-IFNg-PE, anti-TNFa-PerCP710, and anti CTLA4-APC.

Statistics

One-way ANOVA with a Dunnett multiple comparison was used to determine significant between each group in GraphPad Prism. All plots show mean ± standard deviation (SD) where * represents $p<0.05$, ** represents $p<0.01$, and *** represents $p<0.001$

Results

Nanoparticle characterization

PLGA nanoparticles loaded with CpG ODN 1826 (TLR9 agonist), 5'ppp-dsRNA (RIG-I agonist), 3'3-cGAMP (STING agonist), and a melanoma peptide (TRP-2 or gp100) were generated by double emulsion (Figure 2.2). Briefly, the polymer in organic solution was probe sonicated with the cargo in an aqueous solution to form an aqueous core surrounded by polymer in organics. An aqueous solution with the surfactant PVA was added to create the double emulsion with an aqueous environment. The nanoparticles size was characterized by Scanning Electron Microscopy (SEM) (Figure 2.2) and Dynamic Light Scattering (DLS). The nanoparticles (NPs) were 258.1 ± 60 nm with a polydispersity index (pdi) of 0.02 in a hydrated

form by DLS. Loading of adjuvants in the NPs was determined by Size Exclusion Chromatography (SEC): 3.7 % of CpG ODN1826, 0.35% 5'ppp-dsRNA, 2.29% 3'3-cGAMP, and 30% melanoma peptide TRP-2.

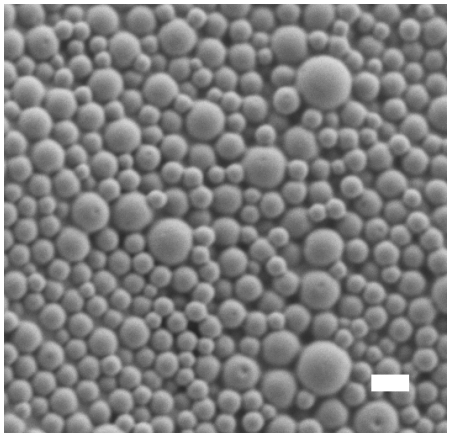

Figure 2.2 iaNP characterization. SEM Scale Bar 500 nm.

Systemic delivery of nanoparticle encapsulated innate agonists induces anti-tumor responses in syngeneic mice

Recent publications have shown the need to utilize drug delivery carrier systems to increase the residency time and potency of therapeutics while limiting systemic toxicity.[37,44] We believe that the short half-life with unencapsulated agonists can be improved with nanoparticles to increase anti-tumor responses. As a result, we wanted to understand the effects of nanoparticles as a carrier system with intratumoral (IT) and intravenous (IV) administration. For these studies, the iaNP contains CpG, RIG-I agonist, STING agonist, and gp100. Melanoma cells were subcutaneously (subQ) injected into the mouse flank. After the tumors were palpable, the mice were treated with PBS vehicle, nanoparticles (NP) only, iaNP, unencapsulated drug combo and the tumor volume was monitored (Figure 2.3A). The tumor size aggressively grew with PBS vehicle when treated with IT injection (Figure 2.3B). There was a moderate decrease in tumor

volume with unencapsulated drug combo with IV administration. However, iaNP treatment IV significantly decreased the tumor volume indicating the presence of nanoparticles encapsulating the drug combo was critical to increase the efficacy of the therapeutic (Figure 2.3B).

When comparing IT injections, aggressive tumors with large tumor volume were seen with the empty NP only and the PBS vehicle. The tumor volumes decreased with treatment where the unencapsulated drug combo performs moderately better than the iaNP when administered IT (Figure 2.3C).

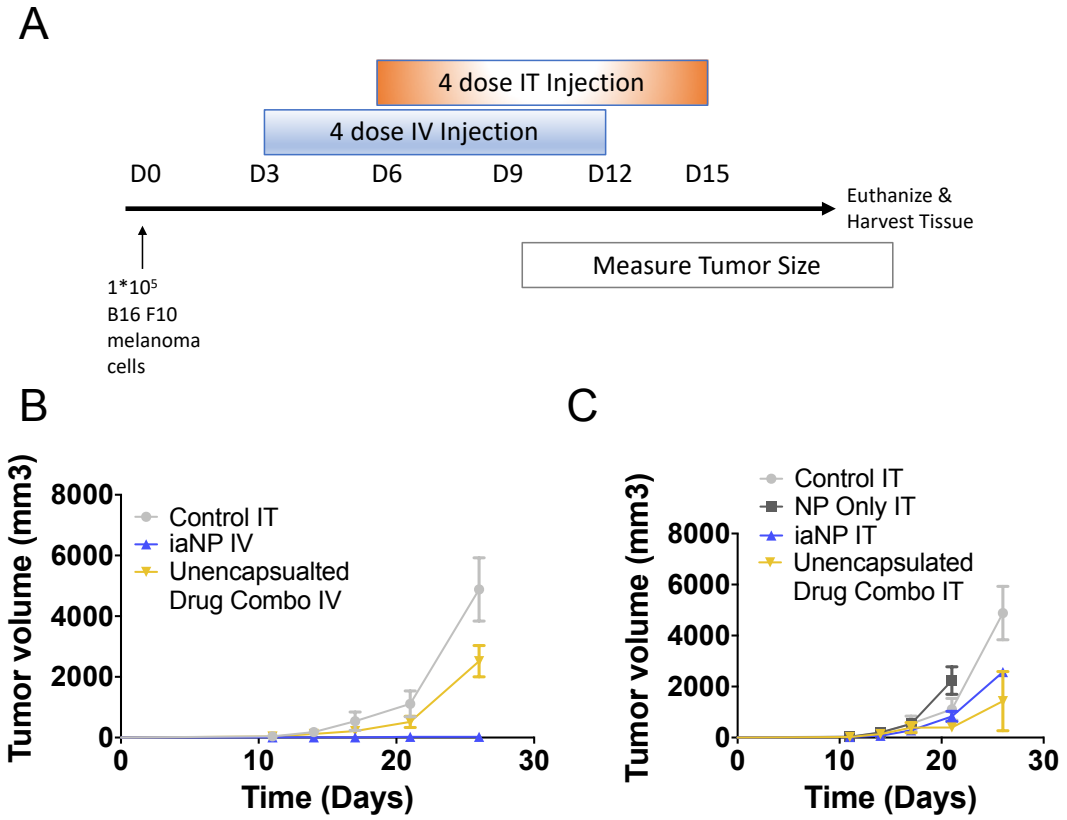

Figure 2.3: **Systemic and intratumoral administered of iaNP reduces tumor volume in asubcutaneous melanoma model.** (A) Timeline (days) for B16F10 melanoma cell subcutaneous inoculation, treatments, and sacrifice for tissue harvest. (B,C) Tumor volume of measured subcutaneous tumor over time (days). Each data point represents one animal. (B) Treatment with intratumorally administration of vehicle PBS, NP only, unencapsulated drug combo, and iaNP. (C) Treatment with intravenous administration of unencapsulated drug combo and iaNP and with intratumoral injection of vehicle PBS.

iaNP reduce tumor burden in lung metastasis model

We hypothesize that systemic delivery of a therapeutic iaNP formulation may have efficacy in a metastatic tumor model. To study this effect, we modeled a metastatic tumor, where B16F10 cells were injected IV through the tail vein. Tumor inoculated mice were treated 4 days later with iaNPs delivered intravenously every 3 days for a total of 3 doses. (Figure 2.4A). The iaNPs contained CpG, RIG-I agonist, STING agonist, and TRP-2 for these studies. Therapeutic efficacy was assessed by harvesting lung tissue to quantify tumor foci. (Figure 2.4C). Remarkably, there was significant reduction in metastatic melanoma foci in the lungs with less than 40 foci observed in iaNP treated animals when compared to saline treated animals that had an average of 116 foci (Figure 2.4B). Modest decrease in tumor burden resulted with NP only treatment while iaNP treatment significantly decreased tumor burden (Figure 2.4B). As a result, the combination of nanoparticles with the drug combo led to an improvement in the metastatic melanoma presence in the lung tissue with 25% of the animals with less than 5 nodules.

iaNP are internalized by antigen presenting cells

iaNP were NPs loaded with innate agonists designed to activate DCs and promote antigen presentation. We studied cellular uptake of iaNP as well as downstream cellular activation. An *in vitro* macrophage cell line, J774, was cultured with fluorescently labeled NPs and imaged with confocal microscopy (Figure 2.5A). Increasing concentrations of nanoparticles resulted in increased nanoparticle positive cells analyzed by flow cytometry (Figure 2.5B). When further investigating the specific cell types that were nanoparticle positive, we saw a significant increase in nanoparticle uptake of 9.35% for classic dendritic cells (cDC), 20.43% for plasmacytoid dendritic cells (pDC) and 32.16% for macrophage with minimal (<0.5%) uptake from T and B cells (Figure 2.5C). From these results we showed selective uptake into these APCs.

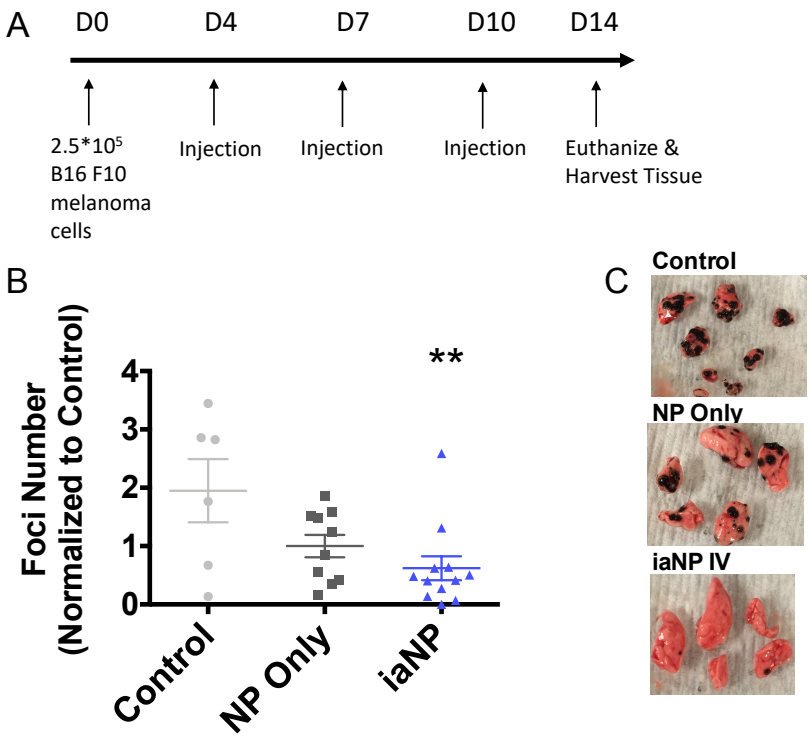

Figure 2.4: **Systemically administered iaNP reduces metastatic melanoma burden in lung tissue.** (A) Timeline (days) for B16F10 melanoma cell intravenous inoculation, treatments, and sacrifice for tissue harvest (B) Number of Lung Foci. Data is normalized to the control and presented as mean ± s.d N ≥ 6. Each data point represents one animal. One-way ANOVA. ** denotes $p<0.01$ (C) Representative lung from WT mouse with melanoma foci with no treatment (control), nanoparticles only and iaNPs.

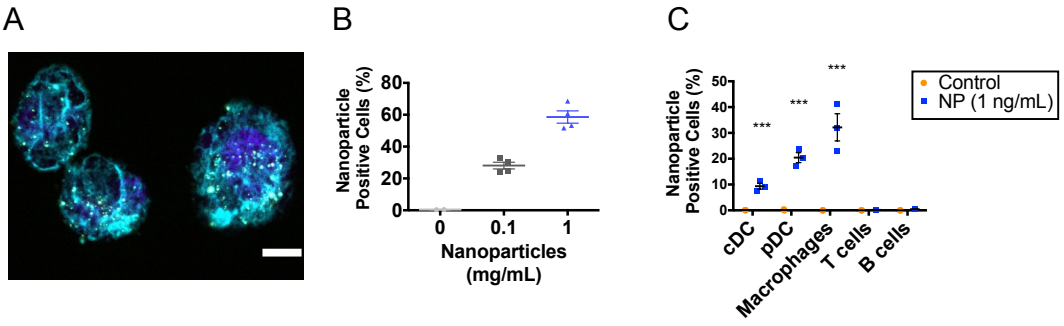

Figure 2.5: **Nanoparticle (NP) uptake by antigen presenting cells *ex vivo*.** Confocal image of (A) J774 cells after 3 hour incubation with fluorescently labeled nanoparticles *ex vivo*. Scale bar 5 µm. Nucleus dapi stain- purple, Actin Phalloidin stain- blue, and nanoparticles in yellow. (B) Concentration dependent nanoparticle uptake into splenocytes by flow cytometry. Data represents mean ± s.d., N=4. (C) Nanoparticle internalization by antigen presenting cells after 3 hours of nanoparticle incubation determine through flow cytometry. Control wells have no nanoparticles present. Data represents mean ± s.d., N=4, Two-way ANOVA, *** denotes $p<0.001$.

Next we investigated the activation of these DCs following iaNP internalization. CD86 is a protein expressed on the surface of APCs that binds to the CD28 ligand on T cells.[45] With iaNP treatment there was a significant increase in broad DC activation compared to control and no change with the NP only group (Figure 2.6A). To further understand the subset of the activated dendritic cells we focused on cDC and pDC. Both cDC1 and cDC2 activated cells increased with iaNP treatment while there was a larger about 2 fold increase in CDC2 compared to control (Figure 2.6B,C). Although generally the pDC population in splenocytes is low, the iaNP significantly increased the number of activated pDC compared to control while no change was present with the NP only group (Figure 2.6D). As B cells play a role in the adaptive immune system and when activated lead to antibody production, we further investigated the effects of iaNP on this cell population. NP only did not alter the population of activated B cells while iaNP significantly increased the number of these B cells (Figure 2.6E). When investigating the effects of iaNP on secretion of cytokines by macrophages, IL-10 amounts were unchanged, but there was a significant increase in IL-12 (Figure 2.6F,G). iaNP were selectively delivered to APCs and induce significant cellular activation as measured by CD86.

We further studied an *in vivo* system where the iaNP, NP only and control were administered IV. Here, iaNP increased APCs in the target tissue, lymph node, along with the spleen while no change was seen in DCs or macrophages in the lung tissue (Figure 2.7). In the lymph node we saw a broad activation of dendritic cell subpopulations (Figure 2.7A). iaNP increased activated cDC1 population by 1.4 fold with no change in the NP only treatment (Figure 2.7B). cDC2 and pDC counts were also significantly increased only in the iaNP treatment group compared to NP only and control (Figure 2.7C,D).

While the spleen monocytes, macrophages, and B cell populations were unchanged with

iaNP treatment, a significant increase in DC populations including cDC1, cDC2 and pDC was seen (Figures 2.7E-K). The B cell population in the splenocytes was not significantly changed with the treatment (Figure 2.7G). While the iaNPs increased activated DC populations, there was no effect on the spleen or lung monocyte populations (Figure 2.7E,L).

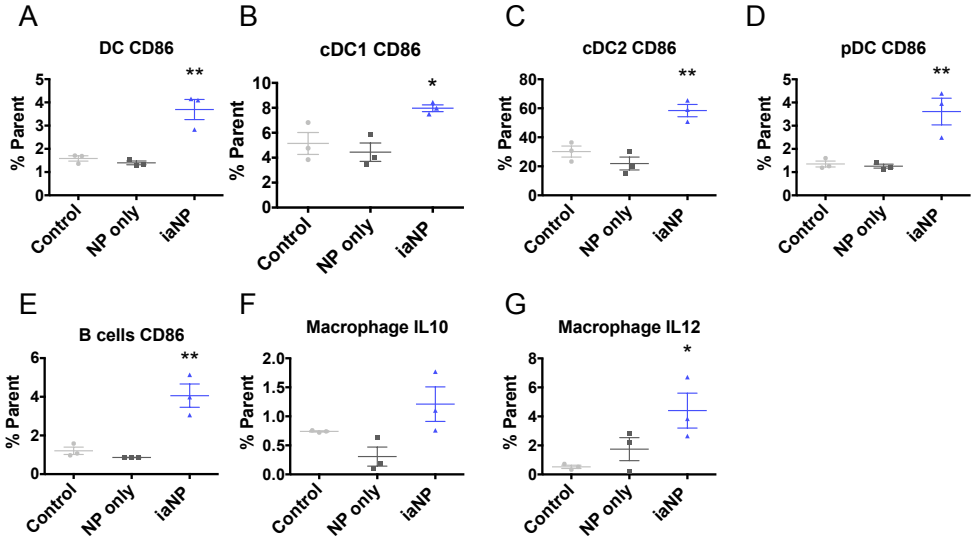

Figure 2.6: iaNP are preferentially internalized by antigen presenting cells *ex vivo*. (a-d) Quantification of Dendritic Cell (DC) populations in splenocytes **(**A) $MHCII^+CD11c^+CD86^+$ dendritic cells (B) $CD11c^+CD8^+CD11b^-CD86^+$ conventional dendritic cells 1 (cDC1) (C) $CD11c^+CD8^-CD11b^+CD86^+$ conventional dendritic cells 2 (cDC2) (D) $CD11c^+CD8^-CD11b^-B220^+MHCII^+CD86^+$ plasmacytoid dendritic cells (pDC) (E) Quantification of $CD3^-B220^+CD86$ B cell population of all $CD45^+$ cells in splenocytes. (F,G) IL-10 and IL-12 expressing macrophages in splenocytes by intracellular cytokine staining. Each data point in the panels consist of one animal. One-way ANOVA, * denotes $p<0.05$, ** $p<0.01$, *** $p<0.001$.

In the lung tissue which was distal to the site of activation of T cells, there was a local increase in macrophages with iaNP (Figure 2.7M). Additionally, in the lung there was no change in IL-10 production from macrophages but a significant increase in IL-12 production was seen similar to the the *ex vivo* experiments (Figure 2.7N,O). These results demonstrate a mechanism by which iaNP delivered systemically induced APC activation in lymph nodes and tumor resident tissues. Furthermore, IL-12 secretory macrophages were induced in the tumor microenvironment, which may also be contributing to the observed anti-tumor efficacy of these iaNPs.

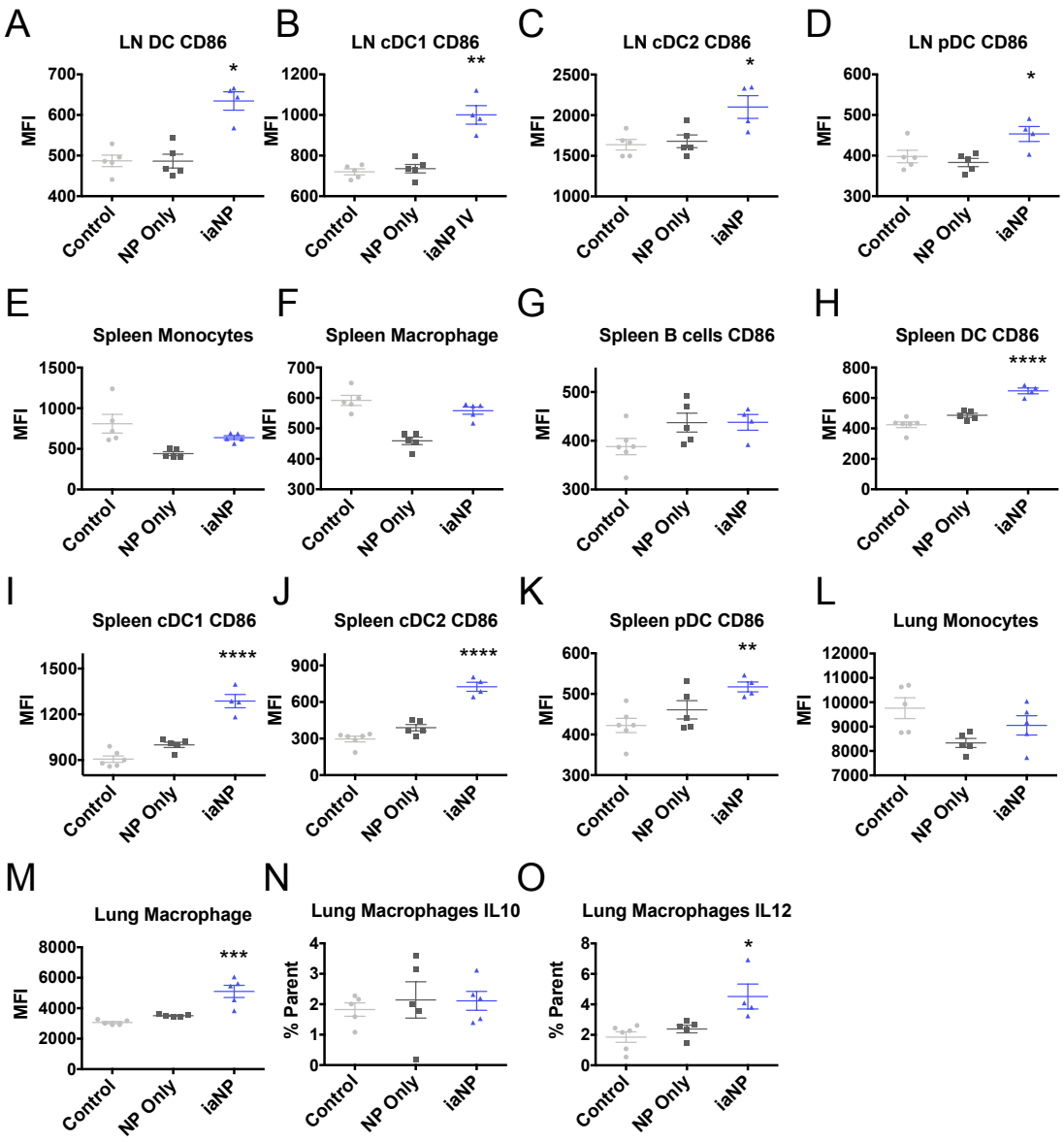

Figure 2.7: Systemically administered iaNP selectively induces DC activation in primary lymphoid tissues. (A-D) Lymph node antigen presenting cell CD86 expression in (A) CD8+ CD11b-CD86+ dendritic cells (B) $CD8^{+}CD11b^{-}CD86^{+}$ conventional dendritic cells 1 (C) $CD8^{-}CD11b^{+}CD86^{+}$ conventional dendritic cells 2 (D) $CD8^{-}CD11b^{-}B220^{+}MHCII^{+}CD86^{+}$ plasmacytoid dendritic cells. Activation of monocytes and macrophages in splenocytes (E) $CD11b^{+}CD64^{+}Ly6c^{+}$ Monocytes (F) $CD11b^{+}CD64^{+}Ly6c^{-}$ $CD64^{+}$ Macrophages (G) Spleen $CD3^{-}B220^{+}CD86^{+}$ B cells (H-K) Antigen presenting cell activation in splenocyte cell populations (H) $MHCII^{+}CD11c^{+}CD86^{+}$ Dendritic cells (I) $CD8^{+}CD11b^{-}CD86^{+}$ cDC1 cells (J) $CD8^{-}CD11b^{+}CD86^{+}$ cDC2 cells (K), $CD8^{-}CD11b^{-}B220^{+}MHCII^{+}CD86^{+}$ pDC cells, (L, M) Activation of monocytes and macrophages in lung cell (L) $CD11b^{+}CD64^{+}Ly6c^{+}$ Monocytes (M) $CD11b^{+}CD64^{+}Ly6c^{-}$ $CD64^{+}$ Macrophages (N,O) IL-10 and IL-12 expressing macrophages in lung cells by intracellular cytokine staining. Data presented as mean ± s.d N=5. Each data point represents one animal. One-way ANOVA. * denotes $p<0.05$, ** $p<0.01$, *** $p<0.001$.

Immune response activated by iaNP

The cytokine levels of iaNP treated mice was analyzed by flow cytometry. Mice were injected IV with B16F10 melanoma on day 0 and treated with control, NP only, or iaNP intravenously over 10 days then sacrificed at day 14 (Figure 2.8A). After sacrifice the tissues were dissociated to single cell level and in aggregate activated with the antigen TRP-2. Here we were able to induce the production of cytokines from TRP-2 sensitive cells across all CD4 and CD8 populations. First, we analyzed the cell and cytokine populations in the target lung tissue where the melanoma foci localize. NP only and iaNP significantly increased IFNγ in the lung population for effector T (Teff) cells compared to control (Figure 2.8B). The iaNP also resulted in an increase in the production of IFNγ in the CD8 cells in the lung (Figure 2.8D). TNFα production for Teff and CD8 populations in the lungs was not changed with treatment (Figure 2.8C,E). We further investigated the effects on distal tissue populations from the site of desired T cell effects, lymph nodes and spleen. iaNP treatment did not alter the Teff cytokine production of IFNγ and TNFα in the lymph node (Figure 2.8F,G). Additionally, we observed a trending increase in CD8+ IFNγ production in the lymph node with iaNP treatment but no change in TNFα production (Figure 2.8H,I). In the spleen tissue interestingly, iaNP significantly decreased the IFNγ and TNFα production of Teff cells with NP only and iaNP treatment (Figure 2.8J,K). Similarly, we saw a decrease in the TNFα production of CD8 cells in the spleen while no difference was seen with the IFNγ production with treatment (Figure 2.8L,M). Importantly, the iaNP treatment did not alter the T regulatory (Treg) cell populations in the LN, spleen, and lung tissues (Figure 2.8N-P). Here we demonstrate not only DC activation, but evidence of the induction of TRP-2 sensitized T cells in the target tumor environment of the lungs.

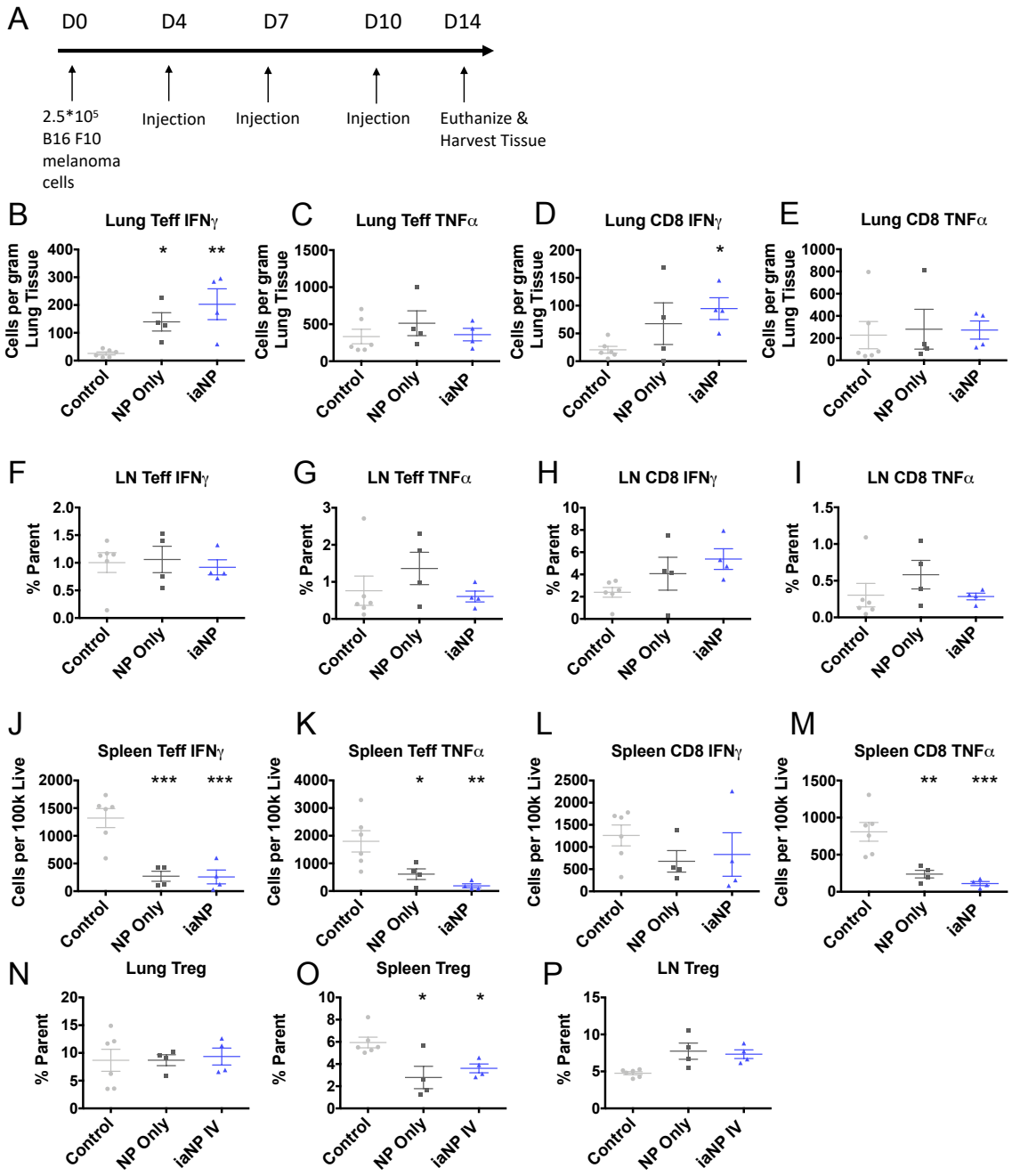

Figure 2.8: **iaNP induces TRP-2 sensitized T cells in the tumor environment in the lungs**. (A) Timeline (days) for B16F10 melanoma cell intravenous inoculation, treatments, and sacrifice for tissue harvest. Cells are stimulated in aggregate with TRP-2 in culture. (B,C) IFNγ and TNFα expressing $CD4^+FOXP3^-$ effector T cells in lung by intracellular cytokine staining. (D,E) IFNγ and TNFα expressing $CD45^+CD8^+$ cytotoxic T cells in lung (F,G) Teff and CD8 IFNγ staining in lymph node cells. (H-J) Teff cells in splenocytes (H) $CD4^+FOXP3^-$ effector T cells (I) IFNγ (J) TNFα. (K-M) CD8 cells in splenocytes (K) $CD45^+CD8^+$ cytotoxic T cells (L), IFNγ (M), TNFα. (N-P) CD4+FOXP3+ Treg cell population in (N) Lung (O) Spleen (P) Lymph Node. Each data point represents one animal. One-way ANOVA. * denotes $p<0.05$, ** $p<0.01$, *** $p<0.001$.

Discussion

Immune agonists are promising potent cancer immunotherapies that can lead to decreased tumor size and metastasis. Combination therapies have shown promising results combining immune stimulators with tumor specific antigens.[40,46–48] CpG ODNs mimic Toll-like receptor (TLR) ligands and are robust immune stimulators and inducers of IFN alpha production and DC maturation.[16] RIG-I agonists have been shown to be a potent pathway to trigger the RIG-I pathway leading to an IFN-mediated antiviral response.[49] STING agonists have been shown to induce production of IFN-b upon binding to STING, enhancing the activation of DCs.[50] We hypothesize that the combination of these innate agonists, TLR9 agonist, RIG-I agonist, and STING agonist, to enhance dendritic cell activation and presentation with a tumor specific antigen to prime T cells to the tumor will lead to enhanced downstream T cell anti-tumor activity. However, the instability, short half-life, and potential systemic toxicity of these small molecules can lead to rapid clearance and decreased therapeutic benefit.[37,44] Additionally, ongoing clinical trials with IT treatment of STING agonists (ClinicalTrials.gov number NCT03010176, NCT03172936) have been promising; however, IT injections are not always feasible based on the tumor type.

Here, we showed coencapsulation of innate TLR9, RIG-1 and STING agonists with tumor specific antigen (gp-100 or TRP-2) in biodegradable PLGA nanoparticles led to a decrease in tumor volume compared to the unencapsulated ligand combination and PBS vehicle when administered IV in a subQ melanoma tumor model. Interestingly, nanoparticle treatment did not increase efficacy with IT treatment. We hypothesize that since when injected IT the drug compounds were localized in the tumor, a therapeutic effect resulted with and without the nanoparticles. However, with IV injection the unencapsulated drugs can be cleared quickly

resulting in decreased efficacy in reducing tumor volume compared to the iaNP formulation.

While treatment with IT injection is possible for subQ melanoma tumors, other examples of cancers such as most solid tumors and blood cancers would not be feasible to perform IT injections. Since iaNP compared to unencapsulated drug combinations administered IV led to a significantly better efficacy, we believe the need to encapsulate the drug combination is essential for efficient delivery of these therapeutics. In a lung melanoma metastasis model, iaNP treatment decreased tumor burden in the lung tissue compared to control and NP only treatment. There was a modest decrease with NP only compared to control which suggests the nanoparticles alone generated a nonspecific immune response leading to a decrease in foci.[51] However, when the nanoparticles were loaded with the immune agonist cocktail, we saw a significant decrease in foci indicating a more specific and potent response.

Next, we wanted to understand the interactions between the nanoparticles and the DC and T cells that led to this therapeutic response. DC presentation and activation is necessary for the subsequent activation of T cells. To prime the immune system the nanoparticles first have to enter the desired APC population. We demonstrated *in vitro* that fluorescently labelled PLGA NPs were selectively internalized by cDC, pDC and macrophages with limited internalization into T and B cells. Once the nanoparticles enter the cells the innate agonists dissociate from the nanoparticle resulting in release of these therapeutics to the desired cell populations with expected downstream activation of these cells.

Overall, *in vivo* we showed an increased activation across DCs with iaNP in lymph nodes and splenocytes. Since, the different populations of DC such as cDC1, cDC2, and pDC can lead to different therapeutic responses we further investigated these cell types in lymph node, spleen, and lung tissue of mice treated with iaNP. Lymph node tissue is a target tissue for DC activation

since it is the main site of interaction with T cells to activate and prime the T cells to the tumor cells. *In vivo*, iaNP treatment increased activated DCs in lymph node and spleen tissue. cDC1 activation results in the cross presentation of antigen through MHCI to activate CD8 T cells to promote T helper type I and NK responses.[52,53] We showed with iaNP treatment, the number of cDC1 activated cells increased in lymph node and spleen tissue. While we also showed an increase with cDC2 cells, these cells are activated by TLRs such as RIG-I and stimulate CD4+ T cells. cDC2 are associated with promotion of Th2 which activate B cells to produce antibodies.[52,53] Here we showed that an activated B cell population moderately increased with iaNP treatment. Since B cells may produce tumor specific antibodies to opsonize tumor cells and trigger NK to kill them this would be an interesting finding to further investigate. pDCs migrate through the blood and lymphoid tissue which stimulates type I interferons resulting in the stimulation and activation of T cells.[52,53] The activated pDC population increased with iaNP treatment in both lymph nodes and splenocytes.

Since 30% of the macrophages internalize nanoparticles, we showed that with iaNP the macrophage population increased in the lung while no difference was seen in the splenocytes. Macrophages produce cytokines IL-10 and IL-12; IL-10 has been shown to limit the extent of activation of innate and adaptive immune cells while IL-12 is a proinflammatory cytokine that is produced by APCs and can further activate NK cells and induce differentiation of CD4 T cells to IFNγ producing T helper 1 effectors.[54] Here we showed that in the lungs there was no change in the IL-10 production and an increase in IL-12 production of macrophages with iaNP treatment *in vivo*. The monocytes did not show an increase in the spleen or lung tissues indicating the main effect with the iaNP was the activation of DCs in the lymph node and spleen along with macrophages in the lungs.

Along with co-encapsulation of the agonists to enhance DC activation and presentation, we encapsulated a peptide specific to melanoma cancer with the goal to sensitize T cells to this peptide allowing for the generation of T cells with this peptide specific receptor on the surface which can then target the specific protein on the melanoma cancer cells. For this analysis we utilized the TRP-2 peptide and the metastatic melanoma model. When cytotoxic T cells are activated, they can target and kill tumor cells with multiple strategies including secretion of cytokines such as IFNγ and TNFα. After culturing the single cells from the tissue with TRP-2 we showed an increase in lung Teff and CD8 production in IFNγ. The T cell activation was minimal in the lymph node compared to the lung which indicated that the T cells have migrated from the lymph node to the site of action where the melanoma was present in the lungs. Interestingly, we also showed a decrease in the Teff IFNγ producing cells indicating these cells have migrated away from the spleen and to the site of action where we saw an increase in IFNγ producing cells.

In summary, we demonstrated nanoparticle loading with an adjuvant agonist cocktail to reduce mouse tumor burden in a subQ and metastatic melanoma mouse model. Nanoparticles were efficiently internalized by APC resulting in activation of these cell populations. APC activation led to an increase in activated T cells primed against the melanoma target to result in an increase in cytokine production and decrease in melanoma. Further investigation of these systemically infused innate activating particles combined with other adaptive immunity therapeutic approaches such as PD-1 combinations is supported by the current studies.

References

1. Marelli, G., Howells, A., Lemoine, N. R. & Wang, Y. Oncolytic viral therapy and the immune system: A double-edged sword against cancer. *Front. Immunol.* **9,** 1–8 (2018).

2. Kaufman, H. L., Kohlhapp, F. J. & Zloza, A. Oncolytic viruses: A new class of immunotherapy drugs. *Nat. Rev. Drug Discov.* **14,** 642–662 (2015).

3. Pol, J., Kroemer, G. & Galluzzi, L. First oncolytic virus approved for melanoma immunotherapy. *Oncoimmunology* **5,** e1115641 (2016).

4. Barve, M. *et al.* Induction of immune responses and clinical efficacy in a phase II trial of IDM-2101, a 10-epitope cytotoxic T-lymphocyte vaccine, in metastatic non-small-cell lung cancer. *J. Clin. Oncol.* **26,** 4418–4425 (2008).

5. Andtbacka, R. H. I. *et al.* Talimogene laherparepvec improves durable response rate in patients with advanced melanoma. *J. Clin. Oncol.* **33,** 2780–2788 (2015).

6. Workenhe, S. T. & Mossman, K. L. Oncolytic virotherapy and immunogenic cancer cell death: Sharpening the sword for improved cancer treatment strategies. *Mol. Ther.* **22,** 251–256 (2014).

7. Diefenbach, A., Jensen, E. R., Jamieson, A. M. & Raulet, D. H. Rae1 and H60 ligands of the NKG2D receptor stimulate tumor.pdf. **413,** 165–171 (2014).

8. Ostroumov, D., Fekete-Drimusz, N., Saborowski, M., Kühnel, F. & Woller, N. CD4 and CD8 T lymphocyte interplay in controlling tumor growth. *Cell. Mol. Life Sci.* **75,** 689–713 (2018).

9. Zanto, T. P., Hennigan, K., Östberg, M., Clapp, W. C. & Gazzaley, A. NIH Public Access. **46,** 564–574 (2011).

10. Thomas, D. A. & Massagué, J. TGF-β directly targets cytotoxic T cell functions during

tumor evasion of immune surveillance. *Cancer Cell* **8,** 369–380 (2005).

11. Lundin, K. U. *et al.* CD4+ T cells kill Id+ B-lymphoma cells: FasLigand-Fas interaction is dominant in vitro but is redundant in vivo. *Cancer Immunol. Immunother.* **53,** 1035–1145 (2004).
12. Gao, F. G. *et al.* Antigen-specific CD4+T-cell help is required to activate a memory CD8+t cell to a fully functional tumor killer cell. *Cancer Res.* **62,** 6438–6441 (2002).
13. Haabeth, O. A. W. *et al.* How do CD4+ T cells detect and eliminate tumor cells that either lack or express MHC class II molecules? *Front. Immunol.* **5,** 1–13 (2014).
14. Russell, S. J. & Barber, G. N. Oncolytic Viruses as Antigen-Agnostic Cancer Vaccines. *Cancer Cell* **33,** 599–605 (2018).
15. Adam Moser, Kevin Range, and D. M. Y. 基因的改变NIH Public Access. *Bone* **23,** 1–7 (2008).
16. Krieg, A. M. & Krieg, A. M. Development of TLR9 agonists for cancer therapy Find the latest version : Review series Development of TLR9 agonists for cancer therapy. *J. Clin. Invest.* **117,** 1184–1194 (2007).
17. Krieg, A. M. Toll-like receptor 9 (TLR9) agonists in the treatment of cancer. *Oncogene* **27,** 161–167 (2008).
18. Hemmi, H. *et al.* A Toll-like receptor recognizes bacterial DNA. *Nature* **408,** 740–745 (2000).
19. Latz, E. *et al.* TLR9 signals after translocating from the ER to CpG DNA in the lysosome. *Nat. Immunol.* **5,** 190–198 (2004).
20. Krieg, A. M. Therapeutic potential of toll-like receptor 9 activation. *Nat. Rev. Drug Discov.* **5,** 471–484 (2006).

21. Usselman, C. W. N. S. S. J. R. B. 乳鼠心肌提取 HHS Public Access. *Physiol. Behav.* **176,** 139–148 (2017).

22. Burdette, D. L. *et al.* STING is a direct innate immune sensor of cyclic di-GMP. *Nature* **478,** 515–518 (2011).

23. Dubensky, T. W., Kanne, D. B. & Leong, M. L. Rationale, progress and development of vaccines utilizing STING-activating cyclic dinucleotide adjuvants. *Ther. Adv. Vaccines* **1,** 131–143 (2013).

24. Yugen Zhang, Laxmi Yeruva, Anthony Marinov, Daniel Prantner, Priscilla Wyrick, Vladimir Lupashin, and U. M. N. The DNA sensor, cyclic GMP-AMP synthase (cGAS) is essential for induction of IFN beta during Chlamydia trachomatis infection. *J Immunol.* **193,** 2394–2404 (2014).

25. Yoneyama, M. & Fujita, T. RNA recognition and signal transduction by RIG-I-like r eceptors. *Immunol. Rev.* **227,** 54–65 (2009).

26. Chen, Y. *et al.* Gene expression profile after activation of RIG-I in 5'ppp-dsRNA c hallenged DF1. *Dev. Comp. Immunol.* **65,** 191–200 (2016).

27. Kotredes, K. P. & Gamero, A. M. Interferons as inducers of apoptosis in malignant cells. *J. Interf. Cytokine Res.* **33,** 162–170 (2013).

28. FAZLE AKBAR, S. M., INABA, K. & ONJI, M. Upregulation of MHC class II antigen on dendritic cells from hepatitis B virus transgenic mice by interferon-γ: abrogation of immune response defect to a T-cell-dependent antigen. *Immunology* **87,** 519–527 (1996).

29. Castro, F., Cardoso, A. P., Gonçalves, R. M., Serre, K. & Oliveira, M. J. Interferon-gamma at the crossroads of tumor immune surveillance or evasion. *Front. Immunol.* **9,** 1–19 (2018).

30. Zevini, Alessandra, Olagnier, David, Hiscott, J. Cross-Talk between the Cytoplasmic RIG-I

and STING Sensing Pathways. *Trends Immunol.* **38,** 194–205 (2017).

31. Ly, L. V., Sluijter, M., van der Burg, S. H., Jager, M. J. & van Hall, T. Effective Cooperation of Monoclonal Antibody and Peptide Vaccine for the Treatment of Mouse Melanoma. *J. Immunol.* **190,** 489–496 (2013).

32. Yang, H. G., Hu, B. L., Xiao, L. & Wang, P. Dendritic cell-directed lentivector vaccine induces antigen-specific immune responses against murine melanoma. *Cancer Gene Ther.* **18,** 370–380 (2011).

33. Manuscript, A. Tryp 2 peptide + RDOTAP. **9,** 261–268 (2013).

34. Bloom, M. B. *et al.* Identification of tyrosinase-related protein 2 as a tumor rejection antigen for the B16 melanoma. *J. Exp. Med.* **185,** 453–459 (1997).

35. Patel, P. M. *et al.* Targeting gp100 and TRP-2 with a DNA vaccine: Incorporating T cell epitopes with a human IgG1 antibody induces potent T cell responses that are associated with favourable clinical outcome in a phase I/II trial. *Oncoimmunology* **7,** 1–15 (2018).

36. Hamdy, S. *et al.* Co-delivery of cancer-associated antigen and Toll-like receptor 4 ligand in PLGA nanoparticles induces potent CD8+ T cell-mediated anti-tumor immunity. *Vaccine* **26,** 5046–5057 (2008).

37. Hanson, M. C. *et al.* Nanoparticulate STING agonists are potent lymph node-targeted vaccine adjuvants. *J. Clin. Invest.* **125,** 2532–2546 (2015).

38. Kim, Hyunjoon, Niu, Lin, Larson, Peter, Kucaba, Tamara A., Murphy, Katherine A., James, Britnie R., Ferguson, David M., Griffith, Thomas S., Panyan, J. Polymeric nanoparticles encapsulating novel TLR7/8 agonists as immunostimulatory adjuvants for enhanced cancer immunotherapy. *Biomaterials* **164,** 38–53 (2018).

39. Shae, D. *et al.* Endosomolytic polymersomes increase the activity of cyclic dinucleotide

STING agonists to enhance cancer immunotherapy. *Nat. Nanotechnol.* **14,** 269–278 (2019).

40. Conniot, J. *et al.* Immunization with mannosylated nanovaccines and inhibition of the immune-suppressing microenvironment sensitizes melanoma to immune checkpoint modulators. *Nat. Nanotechnol.* **14,** 891–901 (2019).

41. Cheng, N. *et al.* A nanoparticle-incorporated STING activator enhances antitumor immunity in PD-L1-insensitive models of triple-negative breast cancer. *JCI insight* **3,** 1–20 (2018).

42. Wang, C., Ye, Y., Hochu, G. M., Sadeghifar, H. & Gu, Z. Enhanced Cancer Immunotherapy by Microneedle Patch-Assisted Delivery of Anti-PD1 Antibody. *Nano Lett.* **16,** 2334–2340 (2016).

43. Jacobson, M. E., Wang-Bishop, L., Becker, K. W. & Wilson, J. T. Delivery of 5′-triphosphate RNA with endosomolytic nanoparticles potently activates RIG-I to improve cancer immunotherapy. *Biomater. Sci.* **7,** 547–559 (2019).

44. Overwijk, Willem, Restifo, N. B16 as a Mouse Model for Human Melanoma. *Curr. Protoc. Immunol.* (2001). doi:10.1002/0471142735.im2001s39.B16

45. Das, M., Shen, L., Liu, Q., Goodwin, T. J. & Huang, L. Nanoparticle Delivery of RIG-I Agonist Enables Effective and Safe Adjuvant Therapy in Pancreatic Cancer. *Mol. Ther.* **27,** 507–517 (2019).

46. Dolfi, D. V. *et al.* Dendritic Cells and CD28 Costimulation Are Required To Sustain Virus-Specific CD8 + T Cell Responses during the Effector Phase In Vivo . *J. Immunol.* **186,** 4599–4608 (2011).

47. Rosalia, R. A. *et al.* CD40-targeted dendritic cell delivery of PLGA-nanoparticle vaccines induce potent anti-tumor responses. *Biomaterials* **40,** 88–97 (2015).

48. Nembrini, C. *et al.* Nanoparticle conjugation of antigen enhances cytotoxic T-cell responses in pulmonary vaccination. *Proc. Natl. Acad. Sci. U. S. A.* **108,** (2011).

49. Lei, Y. M. K., Lekha, N. & Alegre, M.-L. HHS Public Access. *Clin. Res. Hepatol. Gastroenterol.* **39,** 9–19 (2015).

50. Binder, M. *et al.* Molecular mechanism of signal perception and integration by the innate immune sensor retinoic acid-inducible gene-i (RIG-I). *J. Biol. Chem.* **286,** 27278–27287 (2011).

51. Jing, W. *et al.* STING agonist inflames the pancreatic cancer immune microenvironment and reduces tumor burden in mouse models. *J. Immunother. Cancer* **7,** 1–18 (2019).

52. Lee, Y., Kwon, J., Khang, G. & Lee, D. Reduction of inflammatory responses and enhancement of extracellular matrix formation by vanillin-incorporated poly(lactic-co-glycolic acid) scaffolds. *Tissue Eng. - Part A* **18,** 1967–1978 (2012).

53. Collin, M. & Bigley, V. Human dendritic cell subsets: an update. *Immunology* **154,** 3–20 (2018).

54. Schlitzer, A. *et al.* Identification of cDC1- and cDC2-committed DC progenitors reveals early lineage priming at the common DC progenitor stage in the bone marrow. *Nat. Immunol.* **16,** 718–728 (2015).

55. Ma, X. *et al.* Regulation of IL-10 and IL-12 production and function in macrophages and dendritic cells. *F1000Research* **4,** 1–13 (2015).

CHAPTER 3: Tissue-Factor Targeted Benzo-Resolvin and Resolvin D1 Loaded Nanoparticles to Locally Deliver Anti-Inflammatory Compounds Following Vascular Intervention

Abstract

Inflammation and plaque rupturing due to atherosclerosis can lead to clot formation and thrombosis. Current strategies to mediate coronary artery disease include balloon angioplasty and stents. However, these techniques have limitations with limited long-term success and occurrence of restenosis. Pro-resolving lipid mediators (SPMs) are naturally produced at inflammation sites and have been shown to play an important role in the anti-inflammatory response. Resolvin D1 (RvD1) and benzo-diacetylenic-17R-RvD1-methyl ester (BDA-RvD1) are part of the SPM family of compounds that have been shown to attenuate inflammation and improve recovery after tissue injury. In this study, we present a biodegradable tissue factor targeting poly (lactic-co-glycolic acid) (PLGA) polymer-based nanoparticles (NP) loaded with RvD1 or BDA-RvD1. We validated the loading and release of RvD1 and BDA-RvD1 from the NPs. RvD1 NPs were biocompatible and attenuated vascular smooth muscle cell (VSMC) migration. Tissue factor targeted NPs increased localization and RvD1 amounts to damaged artery regions where the epithelial cell layer was disrupted, and tissue factor was exposed. BDA-RvD1 NP increase tissue concentrations compared to BDA-RvD1 gel. Our results demonstrate a materials-based approach to achieve increased local concentrations of anti-inflammatory drug loaded NP to target damaged regions in the arterial wall.

Introduction

Cardiovascular disease is one of the leading causes of death in the world.[1] Atherosclerotic disease chronic inflammation of the artery walls resulting in plaque formation. Rupturing of the plaque in the arteries exposes tissue factor, leading to coagulation cascades and clot formation resulting in thrombosis and acute coronary syndromes.[2] Patients with chronic inflammatory disease such as cystic fibrosis and asthma have decreased levels of pro-resolving lipid mediators (SPMs).[3,4] These SPMs are produced naturally in the body as a key regulator of the anti-inflammatory response.[5]

SPMs derived from ω-3-poly-unsaturated fatty acids are enzymatically oxygenated lipid mediators that function to reduce inflammatory response. [6] Resolvin D1 (RvD1) and benzo-diacetylenic-17R-RvD1-methyl ester (BDA-RvD1) are part of the class of SPMs which have been shown to play an active role in reduction of inflammation in a variety of diseases such as colitis, periodontitis, and lung injury.[7] SPMs have been shown to regulate not only the innate phagocyte response for acute inflammation but also regulates adaptive responses through cytokine regulation of innate lymphoid, natural killer, T, and B cells which have a SPM receptor.[8] RvD1 is derived from docosahexaenoic acid (DHA) that is formed in inflammatory exudates. RvD1 has been shown to halt neutrophil migration and protect against polymorphonuclear neutrophil granulocyte-mediated ischemia-reperfusion injury.[8,9] However, delivery of RvD1 has been challenging due to the instability of the compound. An analog, BDA-RvD1 has been developed to increase chemical stability and reduce metabolism which is a major pathway that reduces the activity of RvD1.[10] Even though the BDA-RvD1 derivation increases stability, the systemic half-life of these small molecules is limited.

Alternatives to small molecules like SPMs include many other interventions for coronary artery disease such as coronary balloon angioplasty, stents and wraps.[11] However, these techniques are invasive and can lead to restenosis which occurs in 30 to 50% of the patients with angioplasty, limiting therapeutic benefits.[12–14] Stents have shown promise over balloon angioplasty with improved luminal diameters, but long term treatment has limited success.[14–16] Nanoparticles (NPs) have developed as a powerful tool to target and deliver therapeutics to desired regions of the body.[17,18] NPs have been shown to allow for protection of small molecules to increase systemic half-life and reduce degradation.[19,20] Strategies have also been developed to target the NPs to desired areas of the body. Targeting NPs allows for a local increase of a therapeutic to the desired region while limiting off target toxic side effects.[21] To target damaged regions of arteries, a peptide was developed to bind to tissue factor (TF).[22] Since the epithelial layer is disrupted in damaged regions, this leads to exposure of the basement membrane protein, TF.

Materials and Methods

Peptide polymer conjugation

The TF targeting peptide sequence was {Lys(FITC)}CGGGKFRVFALTR while a randomized sequence of the same amino acids was used for the nonsense or nontargeting peptide sequence control {Lys(FITC)}CGGGARVFTFRLK.[22] The TF targeting peptide and nonsense peptide were first conjugated to PLGA-PEG-maleimide 10k-5k (PolySci Tech). Two different molar ratios were tested (2:1 and 5:1 of peptide to PLGA-PEG-maleimide polymer ratio) where the peptide was added to the PLGA-PEG-maleimide (30 mg/mL) in DMF with 6% v/v Et_3N. The mixture was reacted overnight to conjugate the thiol of the cysteine on the peptide to the PLGA-PEG-maleimide. The DMF was evaporated by high spin vacuum. Samples were stored at -20°C.

Nanoparticle fabrication

PLGA NPs with a diameter of 250 nm were fabricated as previously described.[23] Briefly, a solution consisting of 100 mg of 100/0, 85/15, 75/25 or 50/50 lactic acid/glycolic acid (L/G) ratio of poly(lactic-co-glycolic acid (PLGA) in dichloromethane (DCM) (50 mg/mL) and poly(2,5-di(hexyloxy)cyanoterephthalylidene (CN-PPV) (3.25 mg/mL) in chloroform (Sigma) was combined. RvD1 (200 ng) or Benzo-RvD1 (2000 ng) were added to NPs in ethanol. For NPs with the peptide on the surface, either targeting or nonsense peptide conjugated to PLGA-PEG-maleimide (20 nmol) was added to 50 mg of PLGA and 3% (w/v) polyvinyl alcohol (PVA) was added at a 1:2 ratio of polymer solution to 3% PVA (v/v). The solution was probe sonicated on ice at 7-8 W or 30 amplitude for 5 seconds on and 10 seconds off for a total of 5 cycles to form stable NPs. The NP solution was diluted 10X with 0.3% (w/v) PVA and stirred for 2 hours to evaporate the DCM. NPs were then purified by a soft wash at 500 rpm to remove large aggregates, then washed 3X with 1% (w/v) PVA to remove small NPs and unencapsulated drug by centrifugation at 12,500 rpm for 10 minutes. The NPs were then lyophilized and stored at -80°C. Prior to studies, the NPs were resuspended in Phosphate Buffered Saline (PBS) or 10% FBS DMEM media.

Release studies

Nanoparticle release was evaluated *in vitro* with PBS as an elution buffer. NPs were incubated with 400 µL of PBS in Eppendorf tubes while shaking at 37°C. At different time points, tubes were scarified and the amount of RvD1 or BDA-RvD1 in the supernatant was measured. Time points measured were 30 minutes, 3 hours, 1 day, 3 days, and 5 days. Samples with RvD1 were analyzed with a 17S-Resolvin D1 enzyme immunoassay kit (Cayman Chemical) and samples with BDA-RvD1 were analyzed by LC-MS/MS.[11] The functional, *in*

vitro and *in vivo* experiments, were performed with 17R-RvD1 which is therapeutically relevant while the release and loading was determined with 17S-RvD1 since the ELISA was specific and more sensitive to 17S-RvD1.

Total drug payload

Maximum loading of RvD1 or BDA-RvD1 in the NPs was measured by dissolving the NPs in 1M NaOH until the solution turned clear. The solution was neutralized with HCL and diluted with 10X PBS. The samples were then run on ELISA for RvD1 and LC-MS/MS for BDA-RvD1.

Cell culture

Viability

Human greater saphenous vein discarded during operations at the University of California San Francisco was used to prepare primary cell cultures of vascular smooth muscle cells (VSMCs), as previously described.[24] Cells between passage numbers 3-5 were used for all experiments. For viability experiments, cells were seeded at $1x10^4$ cells and incubated with NP loaded with RvD1 and RvD1 only at different concentrations, along with a no treatment group. Treatment continued for 24 hours prior to performing the PrestoBlue viability assay. The media or buffer was removed and PrestoBlue cell viability Reagent (Invitrogen) was added to the wells for 10-minutes at 37°C. The absorbance was read at 570 nm. Wells without NPs or RvD1 were used as controls.

Migration assay

VSMCs were seeded and grown to confluency on 24-well plates with 10% FBS DMEM and serum starved overnight. A scratch was made in the well with a sterile pipette tip and imaged. An agonist containing platelet-derived growth factor homodimer BB (PDGF-BB) (10

ng/mL) was added to all the wells to increase migration. The wells were imaged again after 12 hours. The migration was compared at 0 hours and 12 hours and distance was calculated using Image J software.

Tissue factor targeting *in vitro*

Peptide loading was determined by quantifying the amount of peptide incorporated in the NPs by using the fluorescein isothiocyanate (FITC) tag on the peptide. The FITC fluorescence was measured on the NPs by using a plate reader at ex/em 490/525 nm.

For tissue factor plate binding assays a 96 well plate was incubated with different concentrations of tissue factor to coat the plate. NPs with TF target peptide or nonsense peptide were incubated in the tissue factor coated wells. The NPs were washed to remove unbound NPs and the fluorescence was quantified on a plate reader at ex/em 490/525 nm.

Tissue factor targeting *In vivo*

Balloon angioplasty was performed on the coronary artery for 10 minutes to create damaged regions of the artery as a model. A no injury control was performed for comparison. Arteries were then incubated with TF target NP or nonsense peptide NP. The artery sections were visualized by microscopy to determine the location of the NPs. Target peptide NP and nonsense peptide NP loaded with RvD1 were incubated in the artery after balloon angioplasty for 10 minutes. After 10 minutes, blood flow was restored. Acute sacrifice was performed after 10 minutes and the amount of RvD1 in the tissue was determined by LC MS/MS. Benzo-RvD1 was quantified in the tissue 10 minutes and 3 days after blood flow was restored by LC MS/MS. Treatment groups include BDA-RvD1 loaded NPs and BDA-RvD1 in a gel.

Statistics

Statistical analysis was performed by a one-way ANOVA with a Dunnett multiple comparison correction to determine significance between groups. Graphs show the mean ± standard deviation (SD) where * represents $p<0.05$, ** represents $p<0.01$, and *** represents $p<0.001$.

Results

Nanoparticle characterization

NPs were fabricated by single emulsion probe sonication. Briefly, the polymer and RvD1 or BDA-RvD1 were dissolved in the organic phase. The organic phase was probe sonicated with the aqueous 3% PVA surfactant phase to make stable NPs. NPs were visualized with SEM and DLS with an average size of 259.6 ± 18.1 and pdi of 0.099 (Figure 3.1A, B).

The loading and release of RvD1 NPs was determined for different L/G ratios of PLGA by ELISA. PLGA with 75/25 of L/G ratio performed optimally with the highest amount of RvD1 loading resulting in an increased amount of RvD1 release over time (Figure 3.1C, D). The loading of RvD1 in the NPs was 0.5 ng of RvD1/mg NP with an encapsulation efficiency of 25%. BDA-RvD1 was encapsulated in 75/25 L/G PLGA at 0.37 ng BDA-RvD1/mg NP. Altering the L/G ratio of PLGA affects the loading and release due to polymer hydrophobicity and to the increased polymer degradation with higher amounts of glycolic acid.[25–27] Interestingly, 75/25 had the highest loading. As a result, with further experiments we chose to use the 75/25 L/G ratio PLGA polymer.

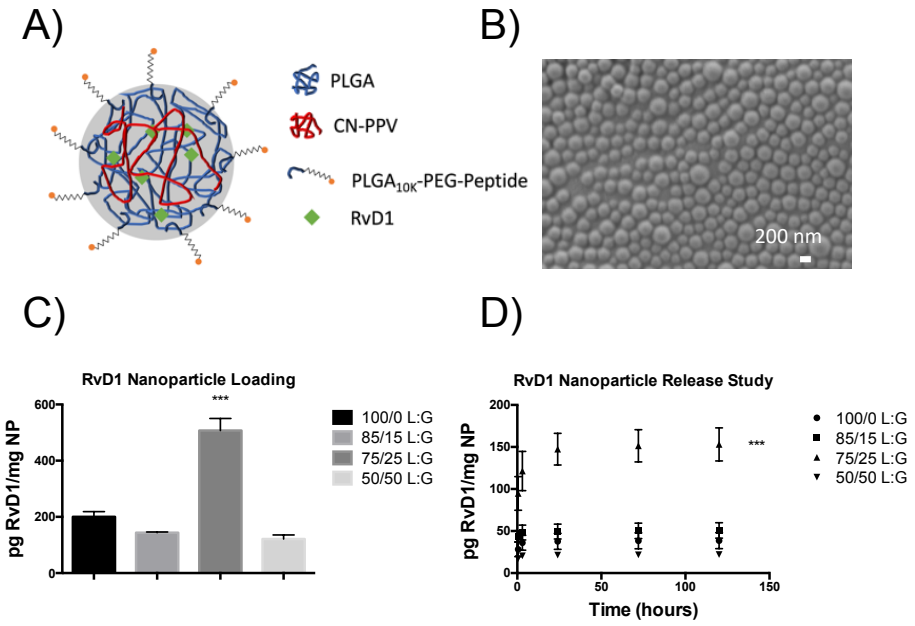

Figure 3.1: **NP characterization.** (A) Schematic representation of RvD1 loaded NP with CN-PPV polymer and surface peptide. (B) Scanning electron microscope image of NPs with 200 nm scale bar. Varying 100/0, 85/15, 75/25, 50/50 L/G ratio of PLGA to optimize (C) RvD1 NP loading (one-way ANOVA, Mean ± SD; n=3, *** $p<0.001$) (D) RvD1 NP release studies (two-way ANOVA, Mean ± SD; n=3, *** $p<0.001$).

Human vascular smooth muscle cell *in vitro* migration assay

RvD1 functions as an anti-inflammatory agent that is utilized during arterial injury.[8] Smooth muscle cells migrate in response to damaged arteries which can lead to intimal hyperplasia.[28] One function of RvD1 is to reduce migration of smooth muscle cells.[29] First, we confirmed that the cell viability of the VSMC was not altered by the NPs (Figure 3.2A). VSMC were cultured in a 24 well plate and a scratch assay was performed to study the migration response of these cells with treatment. RvD1 NP at 8.3 mg/mL, which based on the loading is equivalent to 10 nM RvD1, decreased migration compared to unloaded NP and similarly to treatment with 10 nM RvD1 (Figure 3.2B). As smooth muscle cells can accumulate at the site of an injury, this can lead to intimal hyperplasia. The ability of the RvD1 to release from the NPs and modulate the migration of VSMC is important.

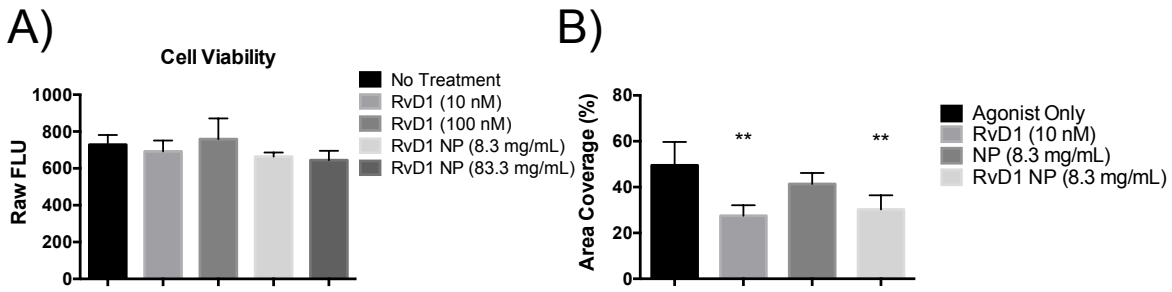

Figure 3.2: **Characterization of nanoparticles in VSMC**. 8.3 mg/mL RvD1 NP based on loading is equivalent to a dose of 10 nM and 83.3 mg/mL RvD1 NP based on loading is equivalent to a 100 nM dose. (A) Biocompatibility studies of the NPs on VSMC for 24 hours with PrestoBlue assay (one-way ANOVA, Mean ± SD; n=3). (B) VSMC migration assay with RvD1 only, NP only, and RvD1 NP compared to a growth factor agonist (one-way ANOVA, Mean ± SD; n=3, ** $p<0.01$).

Peptide targeting nanoparticles to tissue factor

Bypass graft failures can lead to atherosclerosis which results in damaged regions of the artery where the epithelial layer is not intact.[30] This leads to arterial exposure to TF. We aim to target this TF to localize the NPs to the damaged regions for local delivery of RvD1 and BDA-RvD1 to these desired areas. Through thiol maleimide conjugation, the peptide with a cysteine handle was attached to PLGA-PEG-maleimide. This was then added to PLGA, CN-PPV, and RvD1 or Benzo RvD1 prior to probe sonication to form the NPs. The peptide was tagged with FITC to quantify the amount incorporated into the NPs. With increasing ratio of peptide to PLGA-PEG-maleimide, the amount of peptide on the NP increases (Figure 3.3A). The nonsense peptide incorporates similarly to the targeted peptide in the NPs (Figure 3.3A). To understand the specificity of the targeted peptide to TF, an *in vitro* TF plate binding assay was performed. The two higher doses of RvD1 loaded NP lead to a significant difference between the TF targeted NP and the nonsense NP (Figure 3.3B). TF targeted NP binding was significantly enhanced compared to nonsense NP with 500 ng and 250 ng of TF coated on the wells (Figure 3.3C).

In vivo targeting was performed by creating a damaged region on the rat artery by angioplasty then incubation of NP with either TF targeting peptide or nonsense peptide. CN-PPV

is a fluorescent polymer that was incorporated in the NP to allow for tracking of the NP in the artery. The damaged region from the angioplasty was visible in the artery where the epithelium was disrupted. TF targeted peptide NP was more localized to the damaged portion of the artery compared to the nonsense peptide NP which was minimally retained (Figure 3.3D). The goal is to localize the therapeutic RvD1 or BDA-RvD1 to damaged artery regions to reduce the inflammation and prevent intimal hyperplasia that could lead to atherosclerosis. In addition, localization to desired regions allows for an increased local dose to improve therapeutic efficacy. The TF targeted peptide compared to a nonsense peptide selectively colocalized with the damaged regions of the artery.

***In vivo* RvD1 and BDA-RvD1**

An *in vivo* injury model represents a more physiological environment to test the NP targeting and RvD1 and BDA-RvD1 delivery to injured tissue. Balloon angioplasty was performed for 10 minutes to create a damaged region of the artery. NPs with the TF target peptide and NPs with the nonsense peptide conjugated to the surface were administered to the damaged region, incubated for 10 minutes then blood flow was restored. Not only were the NPs with the TF targeting peptide highly localized to the artery compared to the nonsense peptide NPs (Figure 3.3D), but there was also more RvD1 present in the TF targeted NPs after acute (10 minutes) sacrifice (Figure 3.4A). BDA-RvD1 NPs were detectable after 10-minute incubation and still after 3 days. When normalizing the BDA-RvD1 by the starting dose there was significantly more BDA-RvD1 present in the NP group compared to the BDA-RvD1 gel group (Figure 3.4B). The gel formulation has been used in animal models to deliver perivascular drug molecules.[31]

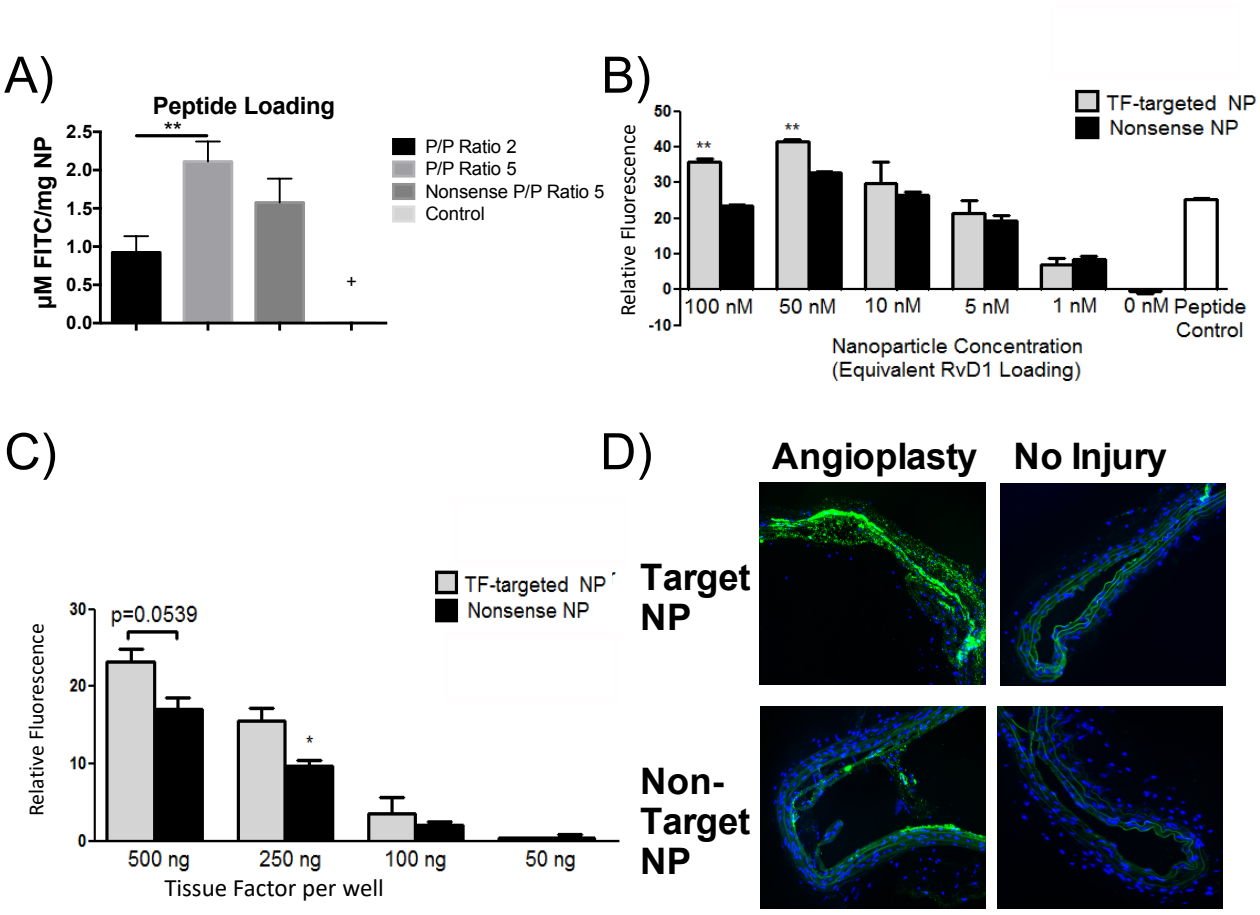

Figure 3.3: **NP with TF targeting peptide increases association with TF and damaged artery regions.** (A) Peptide loading characterization with a peptide/polymer (P/P) ratio of 2 and 5 for the target peptide and a ratio of 5 for the nonsense peptide/polymer ratio. + control well has no detectable fluorescence signal (one-way ANOVA, Mean ± SD; n=3, **p<0.01). TF coated plate with TF targeted NP and nonsense NP altering (B) NP concentration or (C) TF amount per well (one-way ANOVA, Mean ± SD; n=3, **p<0.01). (D) *In vivo* artery with damaged regions by angioplasty compared to no injury between TF targeted NP and non-targeted or nonsense NP.

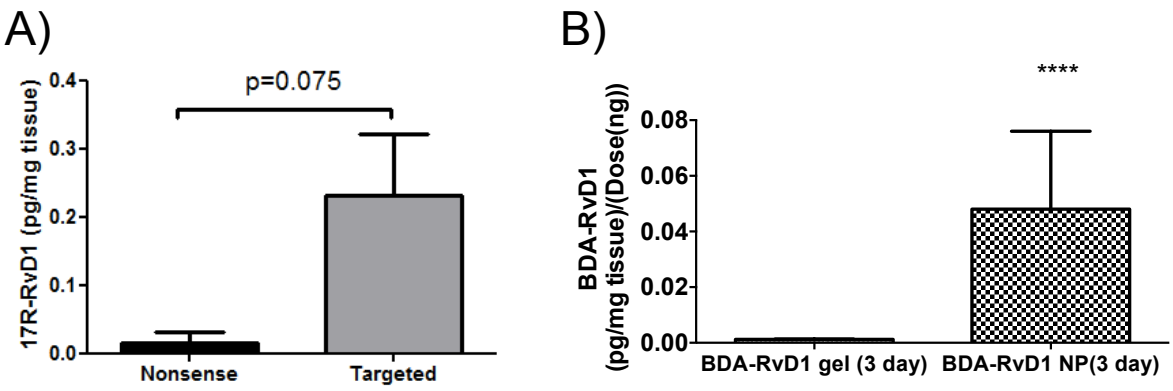

Figure 3.4: ***In vivo*** **drug quantification by LC MS/MS.** (A) Upon administering the nonsense and targeted RvD1 loaded NP, the tissue was sacrificed 10 minutes later and the RvD1 concentrations were measured (one-way ANOVA, Mean ± SD). (B) Amounts of BDA in tissue when BDA-RvD1 was administered by gel and NP after 3 days (one-way ANOVA, Mean ± SD, **** $p<0.0001$, n =3).

Conclusions

The importance of targeting and local concentration of a therapeutic molecule to damaged regions of the artery is well recognized in the cardiovascular field. Current clinical techniques focus on coronary balloon angioplasty and stents. However, these are invasive and can be difficult to administer. There is a critical need for development of strategies to locally release therapeutics in targeted damaged regions. Here, a materials-based approach was applied to study the effects of tissue factor targeted nanoparticles loaded with either RvD1 or BDA-RvD1 along with CN-PPV, a fluorescent polymer for visualization, on damaged regions of arteries. We demonstrated the NPs can be loaded with either RvD1 or BDA-RvD1 in a single emulsion to form stable NPs. With the addition of CN-PPV the NPs could be visualized by microscopy to study the localization and distribution of the NPs after treatment. A peptide that targets TF was conjugated to the surface of the NPs, allowing for local delivery to damaged arteries where TF was exposed, with the goal to maximize drug release in desired areas while limiting off target toxic effects. After an injury to the artery, more RvD1 was present in the

tissues when dosed in a NP formulation with a TF targeting peptide compared to a nonsense peptide. Additionally, in the presence of the NP the BDA-RvD1 amount in the tissue was significantly greater than the gel formulation. We believe this approach can be utilized to target particular regions of the artery to locally delivery a stable therapeutic compound. Future work will continue to characterize the effects of the NPs and optimize the response in the injury model.

References

1. Mc Namara, K., Alzubaidi, H. & Jackson, J. K. Cardiovascular disease as a leading cause of death: how are pharmacists getting involved?. *Integr. Pharm. Res. Pract.* 8, 1–11 (2019).
2. Badimon, L., Padró, T. & Vilahur, G. Atherosclerosis, platelets and thrombosis in acute ischaemic heart disease. *Eur. Hear. J. Acute Cardiovasc. Care* 1, 60–74 (2012).
3. Duvall, M. G., Krishnamoorthy, N. & Levy, B. D. Non-type 2 inflammation in severe asthma is propelled by neutrophil cytoplasts and maintained by defective resolution. *Allergol. Int.* 68, 143–149 (2019).
4. Eickmeier, O. *et al.* Pro-resolving lipid mediator Resolvin D1 serves as a marker of lung disease in cystic fibrosis. *PLoS One* 12, 1–12 (2017).
5. Wang, R. X. & Colgan, S. P. Special pro-resolving mediator (SPM) actions in regulating gastro-intestinal inflammation and gut mucosal immune responses. *Mol. Aspects Med.* 58, 93–101 (2017).
6. Bannenberg, Gerard, Serhan, C. N. Specialized Pro-Resolving Lipid Mediators in the Inflammatory Response: An Update. *Biochim Biophys Acta.* 1801, 1260–1273 (2010).
7. Gu, Z. *et al.* Resolvin D1, resolvin D2 and maresin 1 activate the GSK3β anti-inflammatory axis in TLR4-engaged human monocytes. *Innate Immun.* 22, 186–195 (2016).
8. Serhan, C. N. & Levy, B. D. Resolvins in inflammation: emergence of the pro-resolving superfamily of mediators Protection versus uncontrolled inflammation: first responders and resolution. *J Clin Invest* 128, 2657–2669 (2018).
9. Kasuga, Kie, Yang, Rong, Porter, Timothy F., Agrawal, Nitin, Petasis, Nicos A., Irimia, Daniel, Toner, Mehmet, Serhan, C. N. Rapid Appearance of Resolvin Precursors in

Inflammatory Exudates: Novel Mechanisms in Resolution. *J Immunol.* 181, 8677–8687 (2008).

10. Orr, S. K., Colas, R. A., Dalli, J., Chiang, N. & Serhan, C. N. Proresolving actions of a new resolvin D1 analog mimetic qualifies as an immunoresolvent. *Am. J. Physiol. - Lung Cell. Mol. Physiol.* 308, L904–L911 (2015).
11. Lance, K. D. *et al.* Unidirectional and sustained delivery of the proresolving lipid mediator resolvin D1 from a biodegradable thin film device. *J. Biomed. Mater. Res. - Part A* 105, 31–41 (2017).
12. Kales, A. & Kales, J. D. Long-term follow-up after percutaneous translumincal coronary angioplasty. *N. Engl. J. Med.* 316, 1127–1132 (1987).
13. Holmes, D. R. *et al.* Restenosis after percutaneous transluminal coronary angioplasty (PTCA): A report from the PTCA registry of the national heart, lung, and blood institute. *Am. J. Cardiol.* 53, 77–81 (1984).
14. Grech, E. D. ABC of interventional cardiology: Percutaneous coronary intervention. I: History and development. *Br. Med. J.* 326, 1080–1082 (2003).
15. Feldman, M. & Cryer, B. A randomized comparison of coronary-stent placement and balloon angioplasty in the treatment of coronary artery disease. *N. Engl. J. Med.* 331, 496–501 (1994).
16. Bakken, A. M. *et al.* Long-term outcomes of primary angioplasty and primary stenting of central venous stenosis in hemodialysis patients. *J. Vasc. Surg.* 45, 776–783 (2007).
17. Friedman, A., Claypool, S. & Liu, R. The Smart Targeting of Nanoparticles. *Curr. Pharm. Des.* 19, 6315–6329 (2013).

18. Jiang, T., Jin, K., Liu, X. & Pang, Z. *Nanoparticles for tumor targeting*. *Biopolymer-Based Composites: Drug Delivery and Biomedical Applications* (Elsevier Ltd, 2017).

19. Kadam, R. S., Bourne, D. W. A. & Kompella, U. B. Nano-advantage in enhanced drug delivery with biodegradable nanoparticles: Contribution of reduced clearance. *Drug Metab. Dispos.* 40, 1380–1388 (2012).

20. Hanson, M. C. *et al.* Nanoparticulate STING agonists are potent lymph node-targeted vaccine adjuvants. *J. Clin. Invest.* 125, 2532–2546 (2015).

21. Dadwal, A., Baldi, A. & Kumar Narang, R. Nanoparticles as carriers for drug delivery in cancer. *Artif. Cells, Nanomedicine Biotechnol.* 46, 295–305 (2018).

22. Morgan, C. E. *et al.* Tissue-factor targeted peptide amphiphile nanofibers as an injectable therapy to control hemorrhage. *ACS Nano* 10, 899–909 (2016).

23. McCall, R. L. & Sirianni, R. W. PLGA nanoparticles formed by single- or double-emulsion with vitamin E-TPGS. *J. Vis. Exp.* 51015 (2013). doi:10.3791/51015

24. Chatterjee, A. *et al.* The pro-resolving lipid mediator maresin 1 (MaR1) attenuates inflammatory signaling pathways in vascular smooth muscle and endothelial cells. *PLoS One* 9, (2014).

25. Lü, J. M. *et al.* Current advances in research and clinical applications of PLGA-based nanotechnology. *Expert Rev. Mol. Diagn.* 9, 325–341 (2009).

26. Swider, E. *et al.* Customizing poly(lactic-co-glycolic acid) particles for biomedical applications. *Acta Biomater.* 73, 38–51 (2018).

27. Amann, L. C., Gandal, M. J., Lin, R., Liang, Y. & Siegel, S. J. In vitro-in vivo correlations of scalable plga-risperidone implants for the treatment of schizophrenia. *Pharm. Res.* 27, 1730–1737 (2010).

28. Wadey, K., Lopes, J., Bendeck, M. & George, S. Role of smooth muscle cells in coronary artery bypass grafting failure. *Cardiovasc. Res.* 114, 601–610 (2018).

29. Miyahara, T. *et al.* D-series resolvin attenuates vascular smooth muscle cell activation and neointimal hyperplasia following vascular injury. *FASEB J.* 27, 2220–2232 (2013).

30. Parang, P. & Arora, R. Coronary vein graft disease: Pathogenesis and prevention. *Can. J. Cardiol.* 25, 57–62 (2009).

31. Wu, B. *et al.* Perivascular delivery of resolvin D1 inhibits neointimal hyperplasia in a rabbit vein graft model Bian. *J Vasc Durg.* 68, 188S–200S (2018).

CHAPTER 4: Conclusions

The work described here designs and implements various drug delivery strategies based on therapeutic characteristics and disease target to improve efficacy. Specifically, the focus was on designing nano- and micro- based delivery systems and utilizing them to increase drug delivery for oral drug administration, cancer immunotherapy, and atherosclerosis. Numerous current drug formulations are small molecules, but these are typically cleared rapidly. Nano- and micro- carriers have been utilized to increase a drug's systemic half-life, reduce degradation and allow for modulation such as adding targeting proteins to the surface.

Here we show for oral drug delivery, hydrogel based microdevices reversibly inhibited the intestinal efflux transporters, P-glycoprotein and Breast Cancer Resistance Protein. The drug delivery system was designed with hydrogel material since PEG hydrogels are non-immunogenetic and biocompatible**.** To prevent the intracellular uptake of the hydrogels while still being able to have the material interact throughout the villus, the delivery system was designed to be micrometer size in diameter. This work builds a foundation for further investigation with this system such as optimizing loading of therapeutics in the microdevices to allow for local release of therapeutics only where the transporters are inhibited, to maximize drug absorption along with further investigating the effects of microdevice size on intestinal retention time.

For cancer immunotherapy, polymer nanoparticles loaded with an adjuvant cocktail including a RIG-I agonist, STING agonist, and TLR9 agonist along with a tumor specific peptide increased APC activation and decreased melanoma tumor size in a subQ model and lung foci number in a metastasis model. This system was designed to activate the immune system with a nanometer size for selective uptake into APCs and loading of therapeutics that once released

would promote not only APC activation but also presentation of the loaded peptide specific to melanoma. Additionally, the polymer was utilized due to its unique characteristic to biodegrade and clear naturally. The iaNPs not only promote APC activation but lead to downstream activation of melanoma sensitive T cells to result in reduction of tumor size and foci. This work builds a base for the benefits of combination and activation of multiple pathways to promote and increase the tumor response. Further optimization could be performed to determine the optimal dose and time frame to maximize the nanoparticle response to the tumor cells.

Lastly, in a system designed to reduce inflammation and damage from atherosclerosis, polymer nanoparticles were able to target damaged artery regions to locally release an anti-inflammatory therapeutic. Successful conjugation of a tissue factor targeting peptide to the surface of the RvD1 and BDA-RvD1 loaded nanoparticles resulted in targeting to damaged regions of the artery where in these regions tissue factor is exposed.

Overall, these studies have developed the foundation for future ability to design drug delivery systems to promote local and targeted therapeutic release to desired regions to limit off target toxic effects. The advantage of the drug carrier systems can apply to many applications based on the desired outcome. Further utilization in industry applications has been limited, partly due to the ability to scale up these systems, but as technology such as the NanoAssemblr Blaze develops to scale up liposomes nanoparticles, I believe these drug delivery systems will be implemented more.

Publishing Agreement

It is the policy of the University to encourage the distribution of all theses, dissertations, and manuscripts. Copies of all UCSF theses, dissertations, and manuscripts will be routed to the library via the Graduate Division. The library will make all theses, dissertations, and manuscripts accessible to the public and will preserve these to the best of their abilities, in perpetuity.

Please sign the following statement:

I hereby grant permission to the Graduate Division of the University of California, San Francisco to release copies of my thesis, dissertation, or manuscript to the Campus Library to provide access and preservation, in whole or in part, in perpetuity.

DocuSigned by:
Elizabeth Levy
72F8DE3E3FC2406...

Author Signature

12/4/2019

Date